Monthly Notices of the ROYAL ASTRONOMICAL SOCIETY

MNRAS **00,** 1 (2022)
Advance Access publication 2022 March 17

https://doi.org/10.1093/mnras/stac744

Close, bright, and boxy: the superluminous SN 2018hti

A. Fiore [1,2★] S. Benetti [2★] M. Nicholl,[3,4] A. Reguitti [2,5,6] E. Cappellaro,[2] S. Campana,[7] S. Bose [8,9] E. Paraskeva,[10,11,12,13] E. Berger,[14] T. M. Bravo [15] J. Burke,[16,17] Y.-Z. Cai [18] T.-W. Chen,[19] P. Chen,[20] R. Ciolfi [2,21] S. Dong,[20] S. Gomez,[22] M. Gromadzki [23] C. P. Gutiérrez [24,25] D. Hiramatsu,[16,17,26,27] G. Hosseinzadeh,[28] D. A. Howell,[16,17] A. Jerkstrand,[19] E. Kankare,[29] A. Kozyreva [30] K. Maguire [31] C. McCully,[16] P. Ochner,[2,32] C. Pellegrino,[16,17] G. Pignata,[5,6] R. S. Post,[33] N. Elias-Rosa,[2,34] M. Shahbandeh,[35] S. Schuldt,[30,36] B. P. Thomas,[37] L. Tomasella [2] J. Vinkó,[37,38,39,40] C. Vogl,[30] J. C. Wheeler [37] and D. R. Young[41]

Affiliations are listed at the end of the paper

Accepted 2022 March 14. Received 2022 March 14; in original form 2021 November 9

ABSTRACT

SN 2018hti was a very nearby ($z = 0.0614$) superluminous supernova with an exceedingly bright absolute magnitude of -21.7 mag in *r* band at maximum. The densely sampled pre-maximum light curves of SN 2018hti show a slow luminosity evolution and constrain the rise time to ∼50 rest-frame d. We fitted synthetic light curves to the photometry to infer the physical parameters of the explosion of SN 2018hti for both the magnetar and the CSM-interaction scenarios. We conclude that one of two mechanisms could be powering the luminosity of SN 2018hti; interaction with ∼10 $M_\odot$ of circumstellar material or a magnetar with a magnetic field of $B_p \sim 1.3 \times 10^{13}$ G, and initial period of $P_{spin} \sim 1.8$ ms. From the nebular spectrum modelling we infer that SN 2018hti likely results from the explosion of a ∼40 $M_\odot$ progenitor star.

Key words: supernovae: general – supernovae: individual: SN 2018hti.

1 INTRODUCTION

It is widely accepted that the explosion of massive stars ($\gtrsim$8 $M_\odot$, e.g. Smartt 2009) is triggered by the gravitational collapse of their cores. This leads to a core-collapse supernova (SN) explosion, whose light curves (LCs) reach an absolute magnitude at maximum usually ranging between −14 and −19 mag (e.g. Richardson et al. 2014; Modjaz, Gutiérrez & Arcavi 2019) in optical bands. These luminosities are suitably explained with the decay of <0.1 $M_\odot$ of ^{56}Ni (e.g. Nadyozhin 1994; Müller et al. 2017; Anderson 2019; Prentice et al. 2019) and with the thermal energy deposited in the progenitor's envelope during the gravitational collapse. The discoveries of superluminous supernovae (SLSNe) with an absolute magnitude even brighter than −21 mag (e.g. Gal-Yam 2012, 2019a; Howell 2017) challenge this standard SN paradigm. In fact, $\gtrsim$5 $M_\odot$ of ^{56}Ni would be required to account for these luminosities (e.g. Kasen, Woosley & Heger 2011; Dessart et al. 2012).

Apart from their exceptional brightness, SLSNe are characterized by their pre-maximum/maximum optical spectra, usually showing a hot ($\gtrsim$15 000 K) continuum. Similar to the classical SNe (Minkowski 1941), SLSNe are subclassified as SLSNe I and SLSNe II depending on whether they are hydrogen deficient or hydrogen rich, respectively (Gal-Yam 2012). In addition, SLSNe IIn are characterized by the presence of multicomponent/narrow Balmer emission lines in their spectra and most likely fill the high-luminosity tail of the luminosity function of SNe IIn (Gal-Yam 2012).

SLSNe I are usually discovered in metal-poor and star-forming host galaxies (Chen et al. 2013, 2017a; Lunnan et al. 2014; Leloudas et al. 2015; Perley et al. 2015; Schulze et al. 2018). They are recognized by the presence of prominent absorptions between 3000 and 5000 Å in their pre-maximum/maximum optical spectra. This is an almost unique feature of SLSNe I, usually identified as the contribution of O II transitions (e.g. Quimby et al. 2011; Mazzali et al. 2016; Gal-Yam 2019b), although this identification has been questioned (e.g. Könyves-Tóth & Vinkó 2020). However, these features were observed also in the SN Ib SN 2008D (Soderberg et al. 2008), and in the recently proposed SN subclass of SNe Icn (Gal-Yam et al. 2021; Pastorello et al. 2021) and in the Type-II SN 2019hcc (Parrag et al. 2021). 15–20 d after maximum luminosity, the spectra of SLSNe I start to remarkably reproduce the behaviour of SNe Ic and SNe Ic broad lined (SNe Ic BL) at maximum luminosity (e.g. Pastorello et al. 2010). Interestingly, recent discoveries of SLSNe I and SNe Ic appear to fill the luminosity gap between these two subclasses (such as the cases of the luminous SNe Ic SN 2012aa, SN 2019stc, Roy et al. 2016, Gomez et al. 2021). The physical explanation linking these SN subclasses is still a matter of investigations (e.g. Zou & Cheng 2018; Blanchard et al. 2019; Lin et al. 2020b). The photometric evolution of SLSNe I is more heterogeneous: LCs of SLSNe I typically evolve either smoothly (e.g. SN 2010gx, SN 2011ke, Pastorello et al. 2010; Inserra et al. 2013) or they can show a complex behaviour with pre-/post-maximum bumps (e.g. SN 2015bn, iPTF15esb, SN 2017gci, SN 2018don, Nicholl et al. 2015b; Yan et al. 2015; Angus et al. 2019; Lunnan et al. 2020; Fiore et al. 2021, see also Hosseinzadeh et al. 2021). Their LCs evolve over a very broad range of time-scales; a diversity which prompted

★ E-mail: achillefiore@gmail.com (AF); stefano.benetti@inaf.it (SB)

the community to propose a slow/fast-evolving subclassification of SLSNe I events, but the discovery of intermediate objects (e.g. Gaia16apd, SN 2017gci, Kangas et al. 2017; Nicholl et al. 2017a; Yan et al. 2017a; Fiore et al. 2021; Stevance & Eldridge 2021) and statistical studies (Nicholl et al. 2015a; De Cia et al. 2018; Lunnan et al. 2018b; Angus et al. 2019) point towards a continuous distribution between the two subcategories.

There is no general consensus about the engine powering SLSNe (see Moriya, Sorokina & Chevalier 2018, for a recent review). Several scenarios have been proposed to explain the huge luminosities of SLSNe I: (i) the magnetar scenario, which considers the contribution of the radiation-dominated wind inflated by a spinning down millisecond magnetar (e.g. Kasen & Bildsten 2010; Woosley 2010; Inserra et al. 2013; Chen et al. 2015, 2017b; Wang et al. 2015; Chen, Woosley & Sukhbold 2016; Nicholl, Guillochon & Berger 2017b; Margalit et al. 2018; Vurm & Metzger 2021); (ii) the interaction of the SN ejecta with shells of circumstellar material (CSM, e.g. Chevalier & Fransson 2003; Chevalier & Irwin 2011; Ginzburg & Balberg 2012; Chatzopoulos et al. 2013; Nicholl et al. 2014, 2020; Smith 2017; Lunnan et al. 2018a, 2020) lost by the progenitor star prior to its explosion via stellar winds or alternatively via the pulsational-pair instability phenomenon (e.g. Woosley, Blinnikov & Heger 2007; Woosley 2017; Renzo et al. 2020); (iii) the pair-instability scenario, where e^+, e^- pair creation in a very massive star (with a He-core mass $64\,M_\odot \lesssim M_{\rm He} \lesssim 133\,M_\odot$, e.g. Heger & Woosley 2002) induces the collapse of the star and triggers a thermonuclear runaway in the core, allowing for a massive production of ^{56}Ni. CSM interaction is usually invoked as the major power source for (SL)SNe IIn (as in the case of SN 2006gy, Smith & McCray 2007; Smith et al. 2007; Agnoletto et al. 2009) as it provides a suitable explanation for the narrow/multicomponent features usually seen in their spectra. SLSNe I LCs can be reasonably well explained by CSM models too (e.g. Chevalier & Fransson 2003; Chevalier & Irwin 2011; Ginzburg & Balberg 2012; Chatzopoulos et al. 2013), although the SLSNe I spectra lack for strong interaction signatures. However, it has been shown (Chevalier & Irwin 2011; Moriya & Tominaga 2012; Smith et al. 2015; Andrews & Smith 2018; Bhirombhakdi et al. 2019) that a buried CSM interaction might suppress these features under specific conditions, e.g. if the SN progenitor star is surrounded by a CSM disc (Smith 2017). The complexities in some SLSNe LCs are also indicative of CSM interaction. While the simplest explanation for these complexities is late-time interaction with shells or clumps of CSM (e.g. Moriya et al. 2018), Metzger et al. (2014) argue that they can be mimicked by the opacity variations due to wind-driven ionization fronts of a millisecond magnetar.

In this work, we present and discuss the spectrophotometric observations of SLSN I SN 2018hti, located at RA $= 03^{\rm h}\,40^{\rm m}\,53.76^{\rm s}$, Dec. $= +11^\circ\,46'37.17''$. SN 2018hti was discovered on 2018 November 1 by the Asteroid Terrestrial-impact Last Alert System (ATLAS) project (Tonry et al. 2018a,b) and initially named ATLAS18yff. It was then classified on 2018 November 6 by Burke et al. (2018) as an SLSN I. Independent spectrophotometric data of SN 2018hti are already presented by Lin et al. (2020a) and imaging polarimetry data of SN 2018hti are presented by Lee (2019). Here, we present the photometric and spectroscopic data of SN 2018hti in Sections 2 and 3, respectively. We discuss in Section 4 the spectrophotometric data of SN 2018hti: in particular, the metallicity measurements of its host galaxy (Section 4.1), the blackbody temperature and radius evolutions (Section 4.2), the photospheric velocity (Section 4.3), some photometric and spectroscopic comparisons of SN 2018hti with a selected sample of SLSNe I (Section 4.4), and finally the suitability of magnetar and of CSM-interaction scenarios for SN 2018hti (Section 4.5).

In the following sections, we will assume a flat Universe with $H_0 = 71 \pm 3\,{\rm km\,s^{-1}\,Mpc^{-1}}$, $\Omega_\Lambda = 0.69$, $\Omega_{\rm M} = 0.31$ (taking an average of H_0 among the estimates provided by Planck Collaboration XIII 2016; Khetan et al. 2021; Riess et al. 2021). Hence, the redshift $z = 0.0614$ (see Section 3) measured with the narrow emission lines from the host galaxy corresponds to a luminosity distance $d_{\rm L} = 271.2^{+12}_{-11}$ Mpc.

2 PHOTOMETRY

2.1 Observations and data reduction

We led the multiband photometric follow-up of SN 2018hti via several facilities. Ultraviolet (*uvw2*, *uvm2*, *uvw1*) and *U*, *B*, *V* imaging was obtained with the *Neil Gehrels Swift* Observatory+UVOT (Gehrels et al. 2004). Optical/near-infrared (NIR) *u*, *B*, *g*, *V*, *r*, *i*, *z*, *J*, *H*, $K_{\rm s}$ photometric follow-up was obtained via the NOT Unbiased Transient Survey[1] (NUTS/NUTS2, Mattila et al. 2016; Holmbo et al. 2019) at the 2.56-m Nordic Optical Telescope (NOT)+ALFOSC/NOTCam at the Roque de los Muchachos Observatory, La Palma (Spain), the 1.82m Copernico Telescope+AFOSC and Schmidt Telescopes at the Asiago Astrophysical Observatory (Italy), the 1.2 m telescope at the Fred Lawrence Whipple Observatory+KeplerCam and the 0.6/0.8-m telescopes at the Post Observatory (CA, USA), and Post Observatory Mayhill (NM, USA). We also include the the Asteroid Terrestrial-impact Last Alert System (ATLAS)-photometry, the early ZTF public photometry available via the IRSA[2] archive and Las Cumbres Observatory (LCO)-network[3] *U*, *B*, *g*, *V*, *r*, *i* photometry. LCO data (Brown et al. 2013) come from the Global Supernova Project. ATLAS- *o* and *c* magnitudes were converted to standard Sloan *g* and *r* filter following Tonry et al. (2018a, cfr. equation 2 therein) and Tonry et al. (2012, cfr. equation 6 and table 6 therein). As the colour transformations used within these equations are determined from a stellar spectral energy distribution (SED), the conversion tends to increase the uncertainty of the resulting magnitudes. Also, at very early epochs the $g - r$ colour was estimated via a colour extrapolation since the coeval *g*, *r*-filter photometry is not available. Lastly, we included the mid-infrared (MIR) photometry observed with the Wide-field Infrared Survey Explorer (WISE) NASA mission in the *W*1 and *W*2 wavelength bands.

Photometry was performed with the ECSNOOPY package[4] (Cappellaro 2014) using the point spread function (PSF) fitting technique. A detailed description of the image-processing procedures can be found in Fiore et al. (2021). In particular, for SN 2018hti we removed the background contamination using the template-subtraction technique in the *u*-, *U*-, *B*-, *g*-, *V*-, *r*-, *i*-, *z*-, *W*1-, *W*2-filter images. This was performed with ECSNOOPY via HOTPANTS (Becker 2015). Suitable deep template *u*-, *U*-, *B*-, *V*-filter frames were obtained at the NOT via NUTS2 on 2020 February 25, namely 414 rest-frame days after maximum light and we used PanSTARRS *g*, *r*, *i*, *z* pre-explosion images as template frames. We assumed that SN 2018hti already faded well below the detection limit and used these frames as templates. The

[1] http://nuts2.sn.ie.
[2] https://irsa.ipac.caltech.edu/.
[3] https://lco.global/.
[4] ECSNOOPY is a package for SN photometry using PSF fitting and/or template subtraction developed by E. Cappellaro. A package description can be found at http://sngroup.oapd.inaf.it/ecsnoopy.html.

$W1$, $W2$ frames used as template frames for the WISE photometry were obtained by the WISE mission on 2018 August 18, 19 (MJD = 58348.35, 58349.47), i.e. before the explosion of SN 2018hti. For the NIR frames, the background level was interpolated with a low-order polynomial since no suitable deep template frame in J, H, K_s band was available. B, g, V, r, i, z magnitudes were calibrated having evaluated the photometric zero-points and colour terms with a sequence of field stars from the Pan-STARRS (Panoramic Survey Telescope and Rapid Response System, Chambers et al. 2016) catalogue. The WISE magnitudes were calibrated with their instrumental zero-points. Calibrated PanSTARRS magnitudes were converted to standard SDSS system following Tonry et al. (2012, see equation 6). u magnitudes could not be calibrated with the SDSS survey as SN 2018hti was located outside of its sky coverage. Hence, we calibrated the u magnitudes of the local field stars against u-band photometry of Sloan standards fields taken on the same photometric night. For U, B, V images the calibration was done after converting the Pan-STARRS magnitudes to Sloan magnitudes as before, and then from Sloan magnitudes to Johnson system following Chonis & Gaskell (2008). NIR magnitudes were calibrated with a local sequence of stars from the Two-Micron All Sky Survey (Skrutskie et al. 2006). *Swift*/UVOT *uvw*2-, *uvm*2-, *uvw*1-, *U*-, *B*-, *V*-filter magnitudes were measured by stacking the layers of the individual observing segments with the task UVOTIMSUM. We then measured the brightness using a 2 arcsec-radius aperture with the task UVOTSOURCE task in HEASOFT version 6.25 ((HEASARC) 2014). To calibrate the *Swift*/UVOT magnitudes, we used the recently updated version (2020 November) of the sensitivity corrections. We also analysed data from the *Swift* X-ray telescope by first stacking all 29 UVOT exposures. The total amount of observing time amounts to 52.3 ks. No source was detected at the location of SN 2018hti. The $3\,\sigma$ upper limit on the 0.3–10 keV count rate at the SN position is 6.6×10^{-4} counts s^{-1}. Assuming a power-law X-ray spectrum and the Galactic column density of 1.6×10^{21} cm^{-2} and the distance given in Section 1, we derive an upper limit on the 0.3–10 keV unabsorbed luminosity of 4×10^{41} erg s^{-1}. This is the maximum mean luminosity the SN could have had during the entire *Swift* campaign. Under the hypothesis that the putative X-ray emission follows the UV emission, we restricted our analysis to a time interval centred on the UV peak time in a ± 6 d around maximum. We selected five observations for a total exposure time of 7.9 ks. The SN is still undetected with a $3\,\sigma$ upper limit on the 0.3–10 keV count rate of 4.7×10^{-3} counts s^{-1}, corresponding to a 0.3–10 keV unabsorbed luminosity of 3×10^{42} erg s^{-1}.

Each instrument used for the observational follow-up has its own instrumental throughput. This difference introduces systematic errors when magnitudes are obtained with multiple instruments. To account for this effect, we compute the B, V, g, r, i S-corrections (Stritzinger et al. 2002) for each instrumental configuration using the observed optical spectra of SN 2018hti (similar to Pignata et al. 2004; Elias-Rosa et al. 2006; Fiore et al. 2021) and propagated this into the calculation of the pseudo-bolometric LC. However, we noticed that this correction does not affect our analysis.

The resulting S-correction for the B, V, g, r, i filters and for each instrumental set-up is shown in Fig. 1. For the u, U, z, J, H, K_s filters (which are not covered by the observed optical/NIR spectra), we repeated the above procedure for a set of blackbody spectra shifted to the observer frame of SN 2018hti. The blackbody spectra have temperatures spanning a range of 8000–25 000 K which broadly agrees with the best-fitting blackbody temperatures of the spectra of SN 2018hti (see Section 4.2). In this way, the S-corrections computed for the blackbody spectra provide an estimate of the S-correction outside the optical range. Unfortunately, this approach does not account for the presence of broad emission lines in the SN spectrum, which may alter the estimate of the S-correction. Synthetic-photometry measurements on the two available UV/NIR maximum/post-maximum spectra of other SLSNe I (Gaia16apd, Kangas et al. 2017, and an NIR spectrum of the SN Ic BL SN 1998bw) show that the S-corrections computed on the spectra agree with those computed on their blackbody fit within $\sim$0.05 mag for the z, J, H, K_s filters. In the u and U bands, the blackbody approximation overcorrects the magnitudes with respect to the spectra of Gaia16apd (probably due to the line blanketing). This is true also for the NOTCam S-corrections calculated on the NIR IRTF+SpeX spectrum. To carefully account for this effect requires a denser and better-sampled spectroscopic follow-up outside the optical range, which at the moment has not been done for SLSNe. We therefore opted for the conservative approach of propagating the maximum S-correction ΔS_{corr} computed for the blackbody fits into the error of the pseudo-bolometric LC calculation (see Section 2.3).

The reduced *uvw*2, *uvm*2, *uvw*1, u, U, B, g, V, r, i, z, J, H, K_s, $W1$, $W2$ magnitudes are reported in Tables A1– A5. The S-corrections S_{corr} and the ΔS_{corr} values are listed in Tables A6–A10.

2.2 K-corrections

We computed the K-corrections of SN 2018hti for the B-, V-, g-, r-, i-filter magnitudes performing synthetic photometry measurements on to the observed-frame ($m_{s,\,obs}$) and rest-frame ($m_{s,\,rest}$) optical spectra (see Section 3). These were performed with the PYSYNPHOT PYTHON package.[5] For each filter and each spectrum, the K-corrections were computed as $K = m_{s,\,obs} - m_{s,\,rest}$ and are listed in Table A11. The measured K-corrections are linearly interpolated to the epochs of the imaging observation and subsequently subtracted from the magnitudes of SN 2018hti as measured on those images. $uvw2$, $uwm2$, $uvw1$, u, U, z, J, H, K_s K-corrections were estimated using the SED blackbody fits in place of the observed spectra.

2.3 Observed and pseudo-bolometric LCs

The UV-optical-NIR observed LCs of SN 2018hti are shown in Fig. 2 and are plotted against the phase corrected for time dilation. To estimate the maximum luminosity epoch, we fit a fourth-order polynomial to the r-band LC and infer a magnitude at maximum $r_{max} \simeq 16.5 \pm 0.2$ mag at MJD = 58 464.5 ± 4.0 (in agreement with the maximum found by Lin et al. 2020a). Given a distance modulus $\mu = 37.17 \pm 0.1$ mag and a Galactic extinction[6] $A_V = 1.280$ mag (Schlafly & Finkbeiner 2011), assuming the extinction law $A_V = 3.1 \times E(B - V)$ (Cardelli, Clayton & Mathis 1988, 1989), the absolute peak r-filter magnitude is $M_r = -21.7 \pm 0.2$ mag. We assume no internal extinction from the host galaxy, supported by the absence of the interstellar Na ID doublet and by the fact that the Hα/Hβ ratio remains similar to the expected value for case-B recombination (Groves, Brinchmann & Walcher 2012).

The earliest ATLAS detection was obtained on 2018 October 22 (MJD = 58 413.54) and the last ATLAS detection limit was exactly 3 d before (MJD = 58 410.54). If we assume that the latter is a genuine non-detection, this provides an estimate of the explosion epoch of

[5] https://pysynphot.readthedocs.io/.

[6] Obtained via the NASA/IPAC Extragalactic Database https://ned.ipac.caltech.edu/extinction_calculator.

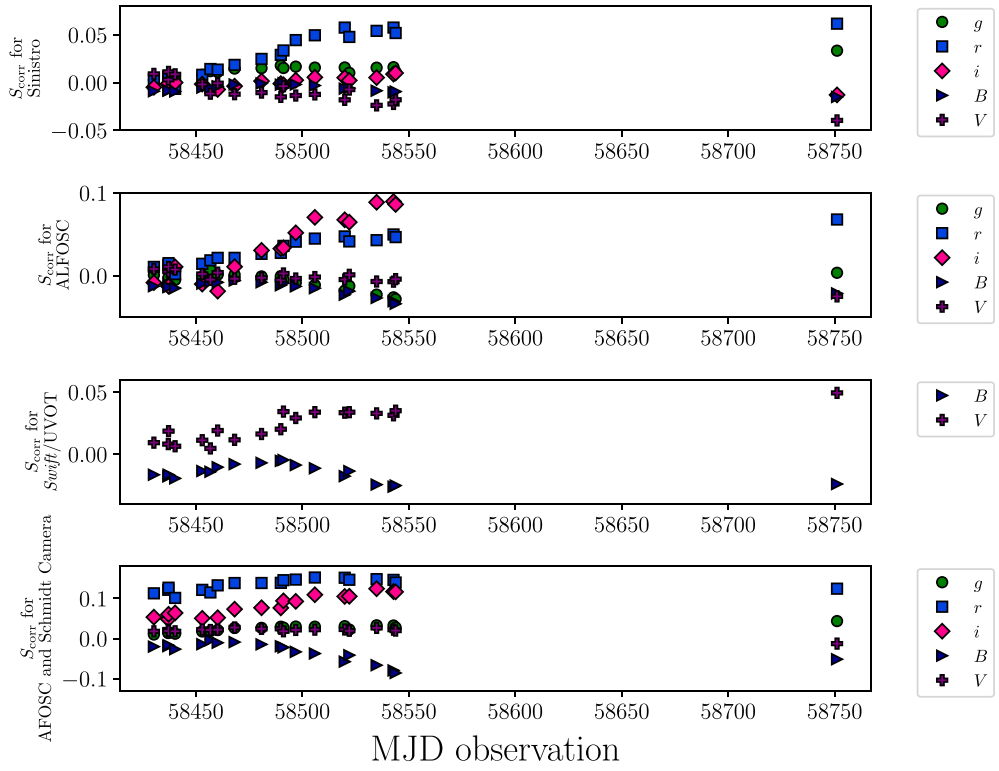

Figure 1. S-correction in *B*-, *V*-, *g*-, *r*-, and *i*-filter passbands for different instruments (Sinistro, ALFOSC, *Swift*/UVOT, AFOSC/Schmidt Camera, in descending order).

MJD = 58 412.04 ± 1.5. With this, the maximum-luminosity epoch implies a rest-frame rise time of $\tau_{\rm rise} = 50 \pm 6$ d, which is typical of the slow-evolving SLSNe I (Inserra 2019). Finally, after ∼100 d from maximum light, SN 2018hti disappeared behind the Sun. For each filter, the LC evolution is characterized by a relatively slow rise to maximum and a post-maximum decline rate of ∼1–2 × $\tau_{\rm rise}$ in each filter. Moreover, the *r*-filter LC apparently shows a levelled off start at earliest phases, which is hard to reconcile with the overall trend of the LC. However, as noticeable in Fig. 2, the very early detections in *r* filter were retrieved by the *o*-filter ATLAS magnitudes whose colour transformations is uncertain. For this reason we also show the observed ATLAS *o*-filter LC in Fig. 3 (top panel), which presents a similar slope change for the first point. To quantify the deviation of the first ATLAS detection from the early behaviour of the LC, we fit a parabola to the ATLAS flux density (expressed in μJy) assuming a flux scaling $F \propto t^2$ (e.g. Riess et al. 1999; Conley et al. 2006). Under this assumption, the first ATLAS point is ∼0.7 mag brighter than the predicted LC. However, the early *r*- and ATLAS *o*-filter detection limits (see Figs 2 and 3) exclude the occurrence of a pre-maximum bump (as in Leloudas et al. 2012; Nicholl et al. 2015b; Smith et al. 2016) up to ∼53 rest-frame days before the estimated explosion epoch. However, we note that the post-maximum epochs ATLAS *o*-filter data fluctuate within ∼0.25 mag in a time-scale ≲10 d. This allows for a 0.25 mag maximum uncertainty for ATLAS magnitudes, which is much less than the 0.7 mag deviation for the first point, making the flat start more credible. Finally, the *K*-corrected and S-corrected *uvw*2, *uvm*2, *uvw*1, *u*, *U*, *B*, *g*, *V*, *r*, *i*, *z*, *J*, *H*, $K_{\rm s}$, *W*1, *W*2 host-template subtracted photometry of SN 2018hti was combined to obtain the pseudo-bolometric LC displayed in Fig. 4 (data are listed in Table A12). This was computed by integrating the multiband photometry neglecting every flux contribution out of the integration boundaries. For SN 2018hti, the epochs of the *r*-band photometry are adopted as reference. The extinction-corrected combined fluxes were finally converted to pseudo-bolometric luminosities by multiplying by $4\pi d_{\rm L}^2$. Similar to the multiband LCs, the pseudo-bolometric LC has a ratio $\tau_{\rm decline}/\tau_{\rm rise} \sim 1.8$ (similar to other SLSNe I, see e.g. Nicholl et al. 2015a).

3 SPECTROSCOPY

3.1 Observations and data reduction

We collected a dense sample of spectra for SN 2018hti starting from MJD = 58 430.2 (2018 November 8), which corresponds to 32 rest-frame days before maximum light.

We led the spectroscopic follow-up via the extended/advanced Public ESO Spectroscopic Survey for Transient Objects (Smartt et al. 2015) (ePESSTO/ePESSTO+), NUTS/NUTS2, with the 1.82-m Copernico telescope at the Asiago astrophysical observatory, Italy, the 2.4m Hiltner Telescope+OSMOS (Ohio State Multi-Object Spectrograph) at the Michigan-Dartmouth-MIT Observatory, and the Hobby Eberly Telescope (HET)+LRS2 (Low Resolution Spectrograph) at the McDonald observatory, Texas. Moreover, we took a pre-maximum (−18 rest-frame days) NIR spectrum via the 3.0-m NASA Infrared Telescope Facility (IRTF)+SpeX (Rayner et al. 2003) and a nebular spectrum on 2019 September 24 (+269 rest-frame days) with the 10.4m Gran Telescopio CANARIAS (GTC)+OSIRIS (Optical System for Imaging and low-Intermediate-Resolution Integrated Spectroscopy, Cepa et al. 2000) at Roque de los Muchachos Observatory. Additional FLOYDS spectra were obtained from FLOYDS on the Faulkes Telescope South (or North) as part of the Global Supernova Project. The instrumental set-ups

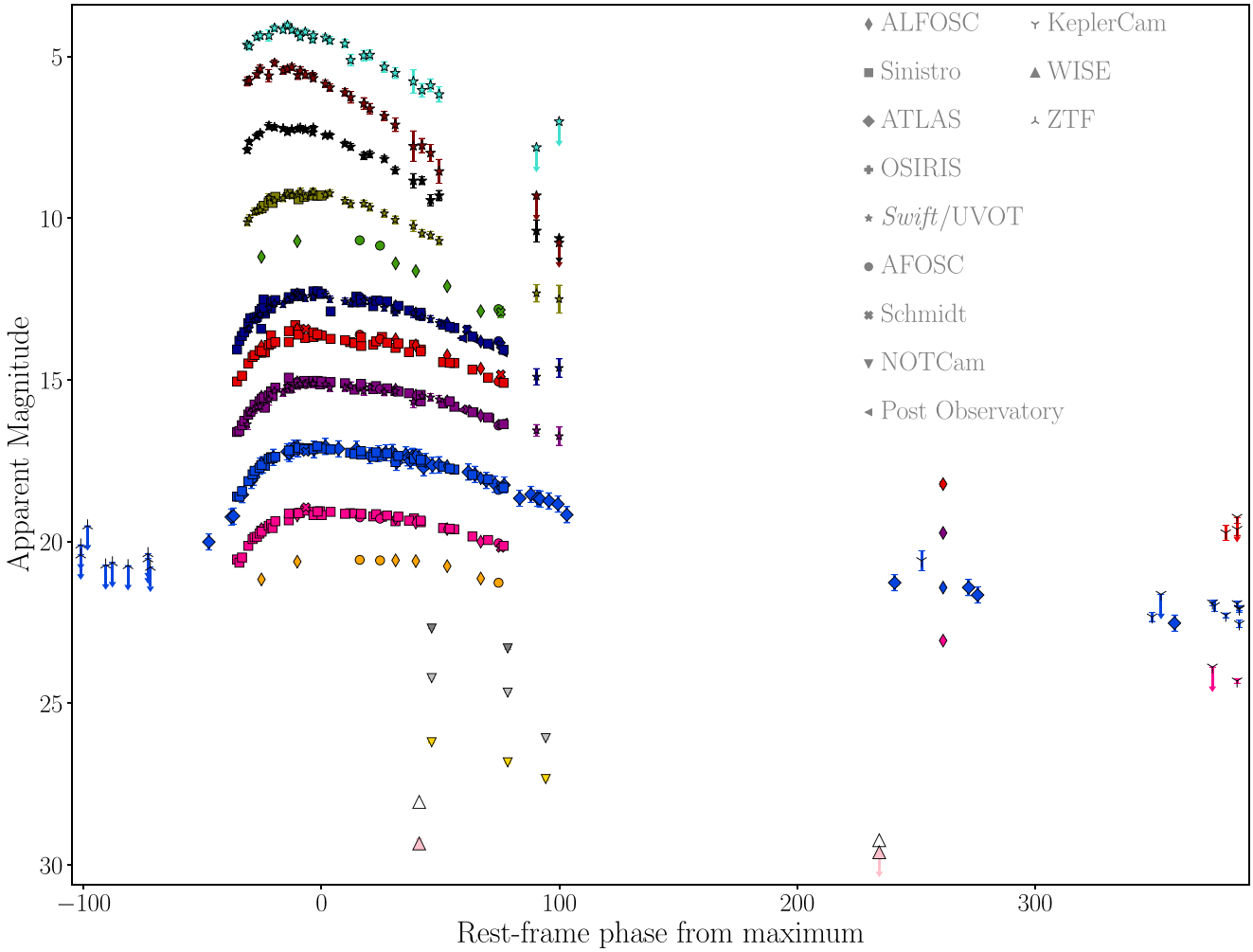

Figure 2. *uvw*2, *uvm*2, *uvw*1, *U*, *u*, *B*, *g*, *V*, *r*, *i*, *z*, *J*, *H*, K_s, *W*1, *W*2 observed LCs of SN 2018hti, respectively, plotted in brown, cyan, black, dark green, dark blue, green, blue, red, purple, magenta, orange, silver, yellow, white, and pink. Data obtained with different instruments are plotted with different markers, as labelled in the top-right corner. Magnitudes are plotted in ABmags.

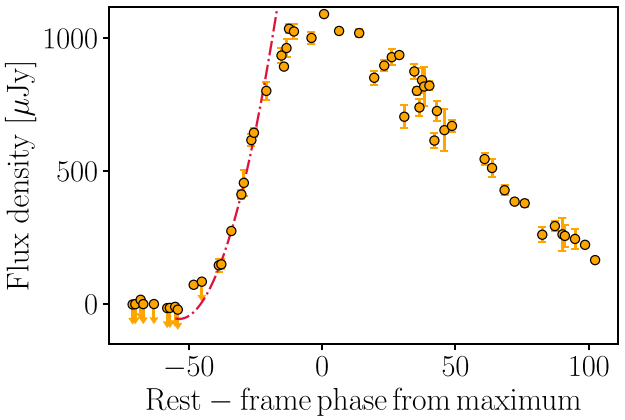

Figure 3. ATLAS-*o* LCs of SN 2018hti (yellow dots) in flux space (expressed in μJy). The early ATLAS LC is fitted with a second-order polynomial (dash–dotted red line).

and the resolution of the spectra presented in this work are listed in Table A13.

The AFOSC, EFOSC2, and GTC spectra were reduced with the standard IRAF procedures. First, the raw bidimensional spectroscopic frames were debiased, flatfielded, and corrected for the cosmic rays contribution with the Laplacian Cosmic Ray Identification package (LACOSMIC, van Dokkum 2001). Then the spectra were extracted along the spatial direction with the IRAF task APALL after having subtracted the background contribution, which was estimated via a low-order polynomial fit. The one-dimensional spectra were wavelength-calibrated against HeAr (for the NTT+EFOSC2), HeNe (for NOT+ALFOSC spectra), NeHgCd (for the 1.82m-Copernico+AFOSC spectra), and HgArNe (for GTC+OSIRIS spectrum) calibration arcs. Then the extracted one-dimensional spectra were flux calibrated via a set of spectrophotometric standard stars observed on the same night and with the same instrumental set-up as the science observations. Using the flux-calibrated standard star spectrum we were able to remove the contribution of the telluric absorption features. Finally, the flux calibration was checked against coeval photometry. The ALFOSC spectra were reduced with

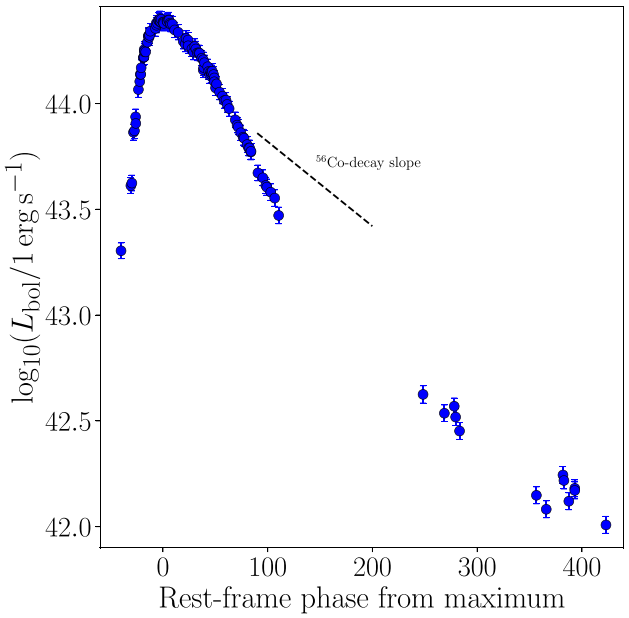

Figure 4. Pseudo-bolometric LC of SN 2018hti (blue dots). The black dashed line indicates the slope of ^{56}Co-decay.

FOSCGUI.[7] The OSMOS spectrum was reduced with the PYRAF-based SIMSPEC[8] pipeline. The LRS2 spectra were reduced with a dedicated IRAF- and PYTHON-based pipeline (as in Yang et al. 2020, see section 2.2.3). FLOYDS spectra were reduced using the FLOYDSSPEC pipeline[9]. The IRTF+SpeX spectrum was reduced utilizing the SPEXTOOL software package (Cushing, Vacca & Rayner 2004).

3.2 Spectral evolution and line identifications

The spectral evolution of SN 2018hti is shown in Fig. 5. Throughout their evolution, the spectra of SN 2018hti show Hβ, Hα, [O III] λ 4959, [O III] λ 5007 narrow emission lines from the host galaxy, which we used to measure the redshift of the host galaxy and to estimate the metallicity at the site of SN 2018hti (see Section 4.1).

The pre-maximum/maximum-light spectra of SN 2018hti present a very hot continuum reaching blackbody temperatures of $\sim$18 000$-$22 000 K. They show the W-shaped O II absorptions between 3500 and 5000 Å. In addition, from the earliest spectrum at phase $-$34 d from the maximum light, a broad feature (FWHM$\sim$15 000–18 000 km s^{-1}) starts to rise in a nearly boxy fashion (see Section 4.5.1). We interpreted this feature as C II λ 6580 (as in Nicholl et al. 2014, see also the discussion in Section 4.5.1). We also mention that the TARDIS modelling of a sample of more than 180 spectra of SLSNe I predicts a C II 6584.70 at a fraction above 50 per cent with a small contribution of Ne I $\lambda\lambda$ 6404.02, 6508.83 (Paraskeva et al. in preparation). This feature does not however reproduce a boxy profile. The early NIR spectrum of SN 2018hti (see Fig. 6) shows an almost featureless continuum with the exception of an emission at a rest-frame wavelength about $\simeq$ 9200 Å which we interpreted as C II λ 9234, similar to the cases of Gaia16apd (Yan et al. 2017a) and to SN 2015bn (Nicholl et al. 2016).

In the spectrum taken 4 d after maximum light, the Fe II emission features are visible in the blue regions, while Mg II begins to be seen in the 15 d post-maximum spectrum. On the same epoch, O I λ 7774 appears in the red end of the spectrum. About 15–30 d after maximum light, the spectrum of SN 2018hti smoothly enters the SN Ic/SNe Ic BL-like phase, similarly to many other SLSNe I (e.g. Pastorello et al. 2010; Inserra et al. 2013; Gal-Yam 2019a). After 39 rest-frame days from maximum an emission shows up at $\sim$6360 Å, which we interpreted as Si II λ 6355. In the 52 d post-maximum spectrum the Ca II NIR $\lambda\lambda\lambda$ 8498, 8542, 8662 triplet becomes visible. After SN 2018hti reappeared from behind the sun, we took the GTC+OSIRIS spectrum on 2019 September 24, 269 d after maximum light. This spectrum is not completely nebular as it displays some residual continuum, which could be however influenced by a residual contribution from the host galaxy (see also Jerkstrand et al. 2017). This phase was referred to as 'pseudo-nebular' by Nicholl et al. (2019).

4 DISCUSSION

Here, we discuss the data presented above. Where possible, we compare data of SN 2018hti with those of other SLSNe I. To do this, we selected a sample of SLSNe I which share some spectrophotometric properties with those of SN 2018hti. We included LSQ14bdq (Nicholl et al. 2015b), SN 2006oz (Leloudas et al. 2012), and DES14X3taz (Smith et al. 2016) since their *r*-filter LCs show a pre-maximum bump. Moreover, SN 2015bn (Nicholl et al. 2016) was prompted as the best-spectral match by GELATO (Harutyunyan et al. 2008). The SLSNe I iPTF13ehe, iPTF15esb, and iPTF16bad (Yan et al. 2015, 2017b) were added to the comparison sample since they show Hα, although at later epochs with respect to maximum light. Finally, we added also a late spectrum of Gaia16apd (Kangas et al. 2017) since few SLSNe I spectra are available at pseudo-nebular/nebular phases.

4.1 Metallicity at the location of SN 2018hti

As mentioned earlier, SLSNe I usually explode in metal-poor, star-forming environments. Several metallicity diagnostics are calibrated from the emission lines emerging from the host-galaxy spectrum. In the case of SN 2018hti, we measured the flux emitted by the [O II] λ 3727, Hβ, [O III] λ 4959, [O III] λ 5007, Hα, and [S II] λ 6717 narrow emission lines emerging from the host galaxy in the nebular spectrum. To measure the flux emitted within the narrow emission lines, we extracted the host-galaxy spectrum close to the position of SN 2018hti by placing the aperture adjacent to the SN itself.

One of these indicators is referred to as R_{23} (Pagel et al. 1979):

$$R_{23} = \frac{([\mathrm{O\,II}]\lambda\,3727 + [\mathrm{O\,III}]\lambda\,4959, 5007)}{\mathrm{H}\beta}\,. \quad (1)$$

Another indicator which is often used is the so-called N2O2 (Kewley & Dopita 2002):

$$\mathrm{N2O2} = \frac{[\mathrm{N\,II}]\lambda\,6584}{[\mathrm{O\,II}]\lambda\,3727}\,. \quad (2)$$

For SN 2018hti, we found $\log_{10}R_{23} = 0.96$ and $\log_{10}(\mathrm{N2O2}) = -1.26$. To measure the metallicity of the host galaxy at the site of SN 2018hti, we evaluated different metallicity estimators

[7] FOSCGUI is a graphic user interface aimed at extracting SN spectroscopy and photometry obtained with FOSC-like instruments. It was developed by E. Cappellaro. A package description can be found at http://sngroup.oapd.inaf.it/foscgui.html.
[8] https://astro.subhashbose.com/simspec/.
[9] https://github.com/svalenti/FLOYDS_pipeline/blob/master/bin/floydsspec/

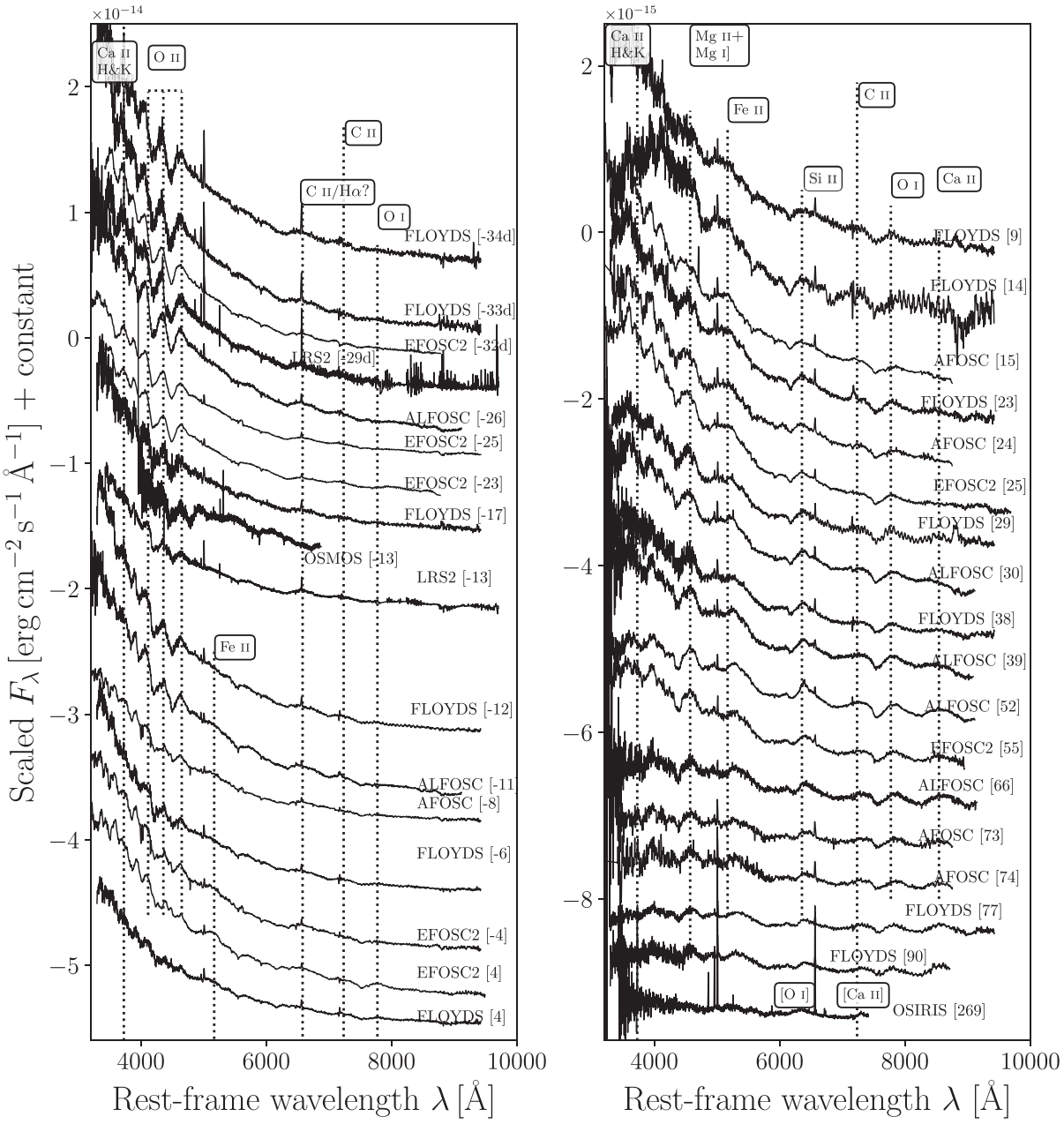

Figure 5. Spectral evolution of SN 2018hti. Spectral line identifications are marked with vertical black dotted lines, and labelled on its right side with the corresponding ion. The rest-frame phase with respect to maximum luminosity is reported on the right side of each spectrum. The left-hand panel shows the spectral evolution of SN 2018hti from −34 to 4 d from maximum luminosity and the right-hand panel shows the remaining spectra up to 269 d after maximum luminosity.

simultaneously due to the tool PYMCZ[10] presented by Bianco et al. (2016). PYMCZ randomly samples a Gaussian distribution whose mean and standard deviation are given by the flux measurements and their uncertainties, respectively. With this tool, it was possible to exploit the D04 (Denicoló, Terlevich & Terlevich 2002), M91 (McGaugh 1991), M08_N2HA, M08_O3O2 (Maiolino et al. 2008), and M13_N2 (Marino et al. 2013) metallicity estimators. Other metallicity estimators calculated by PYMCZ are excluded from our analysis since they are not suitable for the case of SN 2018hti. In particular, Z94 (Zaritsky, Kennicutt & Huchra 1994) is valid only for the upper branch of the $\log_{10}R_{23}$ scale.[11] Also, the KD02 and KK04 methods should only be used for $\log_{10}(\mathrm{N2O2}) > -1.2$. The results are shown in the boxplot in Fig. 7 and are summarized in Table 1. As expected, the results point towards a metal-poor site with $12 + \log_{10}(\mathrm{O/H}) \approx 8.17$, which corresponds to a metallicity $Z \approx 0.3\ Z_\odot$ (assuming $12 + \log_{10}(\mathrm{O/H}) = 8.69$ for the solar metallicity, Asplund et al. 2009). This estimate nicely agrees with the results obtained by Lin et al. (2020a).

[10]The package can be found at https://github.com/nyusngroup/pyMCZ.

[11]The upper branch metallicity scale is defined by the condition $\log_{10}R_{23} < 0.9$ (e.g. Kewley & Ellison 2008).

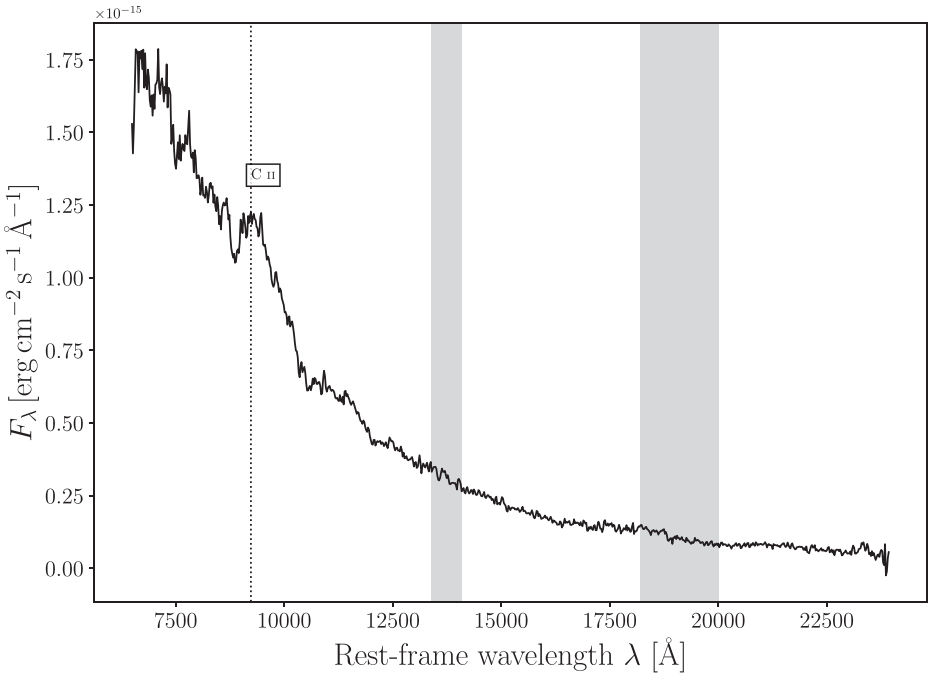

Figure 6. The IRTF+SpeX spectrum of SN 2018hti (black solid line). The black dotted line marks the C II at $\lambda = 9234$ Å line identification and the shaded grey areas mark the spectral regions corrected for telluric absorptions.

Moreover, we estimated the star formation rate (SFR) of the host galaxy of SN 2018hti based on the measurements of the flux emitted by the reddening-corrected narrow H α using equation 2 of Kennicutt (1998). The derived SFR is $\sim 0.3\,M_\odot\,yr^{-1}$, similar to the SFRs measured by Chen et al. (2017a) for a sample of galaxies hosting SLSNe I and comparable to the SFR of the Large Magellanic Cloud (Harris & Zaritsky 2009). Finally, we compared the values of SFR and metallicity of SN 2018hti with those of the comparison sample (see Table 2). Given the intrinsic uncertainty of these measurements, the selected SLSN-I sample seem to share similar environments, with the exception of SN 2015bn, which has an SFR about an order-of-magnitude lower than the others. However, as pointed out by Nicholl et al. (2015b), modelling the host-galaxy SED and estimating the median stellar mass and the age of the stellar population returns a higher SFR value of $0.55 \pm 0.18\,M_\odot\,yr^{-1}$ for SN 2015bn. Also, the SFR value reported for LSQ14bdq is an SFR limit (see also section 4 in Chen et al. 2017a).

4.2 Blackbody temperature and photospheric radius

We obtained the time evolution of the blackbody temperatures by fitting a blackbody curve to the spectra. This allow us to avoid the contribution of the spectral lines in the fitting procedure by excluding the line-contaminated regions from the fit domain. The comparison of the temperature evolution of SN 2018hti with SN 2015bn (Nicholl et al. 2016), SN 2006oz (Leloudas et al. 2012), iPTF13ehe (Yan et al. 2015, 2017b), iPTF15esb (Yan et al. 2017b), iPTF16bad (Yan et al. 2017b) is shown in Fig. 8 (left-hand panel). The data of SN 2006oz are relatively dispersed, but are useful for an order-of-magnitude comparison. The temperature evolution of SN 2018hti is essentially monotonic and is very similar to the case of SN 2006oz, the steepest of the sample. SN 2018hti and SN 2006oz appear to have the hottest photospheres among the SLSNe I sample. However, the scarcer sampling of the blackbody temperatures of iPTF13ehe and iPTF16bad do not allow to properly compare them with SN 2018hti. In particular, both SN 2015bn and iPTF15esb reach a 'temperature floor' (Nicholl et al. 2017b) of 5000–8000 K after ∼50–80 d after maximum luminosity (Fig. 8) similar to the sample analysed by Inserra et al. (2013) (see also Nicholl et al. 2017b). In the case of SN 2018hti it is unclear whether or not the temperature evolution actually settles on a plateau at that phase.

We also determine the evolution of the photospheric radius (Fig. 8, right-hand panel) R_{ph} using the Stefan–Boltzmann law, where we used the pseudo-bolometric luminosities shown in Fig. 4. To compare the more sparsely sampled spectroscopic epochs with those of the pseudo-bolometric luminosities, we fit the blackbody temperatures with a second-order polynomial. The photospheric radius of SN 2018hti monotonically grows to a maximum value of $\sim 9 \times 10^{15}$ cm in 100 d, which is about ∼50 d later the maximum bolometric luminosity. It then recedes at a rate of about $7 \times 10^{13}\,cm^2\,day^{-1}$, which is similar to the average growth rate. Overall, the photospheric-radius evolution is consistent with the expansion radius determined from expansion velocity derived from some spectral lines (see Section 4.3) except for the time interval between −26 and 35 rest-frame days from maximum (see Fig. 8, right-hand panel). However, given the huge uncertainties, this should be considered only as an order-of-magnitude comparison. In the same figure we also show the photospheric-radius evolution of SN 2006oz. The photosphere of SN 2006oz seems less extended than that of SN 2018hti. In fact, given that both of them have a comparable photospheric temperature, SN 2006oz is about ∼0.5 mag fainter than SN 2018hti (see also Sec. 4.4).

4.3 Photospheric velocity

The photospheric velocity of SN 2018hti is measured via the O II λ 4357, O II λ 4650, and O I λ 7774 P-Cygni absorption features present in the spectra. In particular, it has been shown that the O I

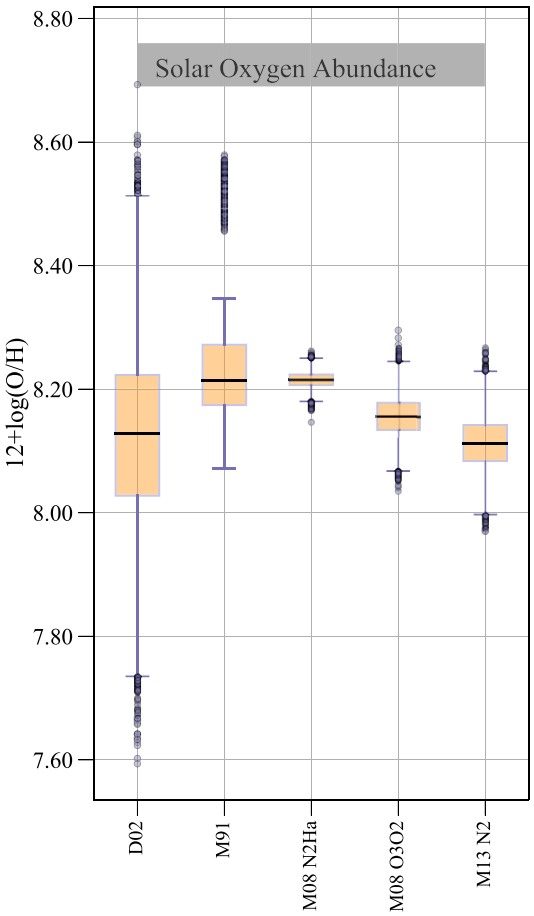

Figure 7. Boxplot obtained with the tool PYMCZ. The orange boxes cover the interquartile range (IQR) for each estimator, and the blue dots deviate from the first and third quartile more then 1.5 × IQR. The grey box broadly corresponds to the solar oxygen abundance.

Table 1. Metallicity estimators provided by the PYMCZ tool for the site of SN 2018hti (see also Fig. 7).

Estimator	$12+\log_{10}$(O/H)
D02	$8.128^{+0.142}_{-0.149}$
M91	$8.214^{+0.123}_{-0.055}$
M08_N2HA	$8.215^{+0.013}_{-0.013}$
M08_O3O2	$8.156^{+0.033}_{-0.033}$
M13_N2	$8.113^{+0.044}_{-0.042}$

λ 7774 feature is a good tracer of the photosphere of the stripped envelope SNe (Dessart et al. 2015). The wavelengths corresponding to the absorption minima were inferred from a Gaussian fit of the absorption features (see Fig. 9). This method is marginally affected by the line blending (Jeffery & Branch 1990) which can substantially bias the velocity measurements (Gal-Yam 2019b). The velocity evolution of SN 2018hti is shown in Fig. 10 (right-hand panel) in comparison with the photospheric velocities of SN 2015bn, iPTF13ehe, iPTF15esb, and iPTF16bad (where the photospheric velocities of iPTF13ehe, iPTF15esb, and iPTF16bad were retrieved based on the Fe II λ 5169). In the case of SN 2018hti, after an initial very steep decline, the velocity evolution settles on an early plateau which starts ∼22 d before maximum luminosity and lasts ∼30 d. Overall, the photosphere of SN 2018hti recedes (in mass coordinates) similarly to SN 2015bn and both of them are much slower than the other SLSNe I of the comparison sample. Finally, we compared the photospheric-velocity evolution of SN 2018hti with the results of the numerical radiation hydrodynamic calculations of Kasen & Bildsten (2010, see also their fig. 2, bottom panel) for a magnetar-powered SN assuming a magnetic field $B_{\rm p} = 0.5 \times 10^{14}$ G, an initial period $P_{\rm spin} = 5$ ms, an ejecta mass $M_{\rm ejecta} = 5\,{\rm M}_{\odot}$, and a kinetic energy $E_{\rm kin} = 10^{51}$ erg. We scaled this solution by a factor 1.37 to almost perfectly fit the measured photospheric velocities of SN 2018hti (see also Section 4.5.2).

4.4 Comparisons with other SLSNe I

We compared the *r*-filter absolute magnitude LC of SN 2018hti with those of the comparison sample (see Fig. 11, left-hand panel). These SLSNe I show an early bump in their LCs and/or spectral signatures that likely involve some ejecta-CSM interaction (i.e. a possible Hα emergence). Interestingly, this sample shares similar evolutionary time-scales (see Fig. 11, left-hand panel) up to ∼80 d after maximum light, even though the absolute peak magnitude spans a range >2 mag.

Three representative spectra of SN 2018hti (at phases −8, +73, +269 d after maximum) are compared with the spectra of LSQ14bdq, SN 2018bsz, DES14X3taz, Gaia16apd, and SN 2015bn (Fig. 12). The spectra of LSQ14bdq, 2018bsz, iPTF15esb, Gaia16apd, DES14X3taz, and SN 2015bn are from WISEREP[12] (Yaron & Gal-Yam 2012). The spectrum of SN 2018hti taken 8 d prior to maximum light is compared with the spectra of LSQ14bdq (at a phase of −15 rest-frame days), SN 2018bsz (at a phase of −6 rest-frame days), and DES14X3taz (at a phase of −21 rest-frame days). At these phases, the O II features in the blue region of the spectrum of SN 2018hti nicely match those of LSQ14bdq, SN 2018bsz, and DES14X3taz. However, in the earliest spectrum of SN 2018bsz the P-Cygni maximum of the O II λ 4650 feature is likely affected by line blending with C II λ 4745 (Anderson et al. 2018). At about 60–70 d after maximum luminosity, the spectrum of SN 2018hti is also similar to the spectrum of iPTF15esb, although the latter shows a more prominent Mg I] λ 4571 and broader Fe-group features at ∼5500 Å. The remarkable resemblance between SN 2018hti and SN 2015bn at about 70 d after maximum suggests that these SNe have similar ejecta velocities (see also Fig. 10) and chemical composition. Finally, the late/pseudo-nebular spectrum of SN 2018hti at 269 d after maximum is compared with the spectra of SN 2015bn and Gaia16apd at a phase +270 and +252 d, respectively. The nebular emission features of SN 2015bn and Gaia16apd are more strongly developed compared to SN 2018hti, although they share some resemblance in the blue region of the spectrum.

4.5 Data interpretation

We considered two different scenarios to interpret the data of SN 2018hti: the magnetar and the ejecta-CSM interaction scenarios. To test the viability of the two hypotheses, we modelled the multicolour LCs of SN 2018hti with the Modular Open Source Fitter for Transients (MOSFIT, Guillochon et al. 2017, 2018). We also used the published radiative-transfer solutions of the SUMO code (Jerkstrand et al. 2017) for the nebular emission of O-zone material

[12] https://wiserep.weizmann.ac.il.

Table 2. Metallicities and SFRs of the SLSNe I of the comparison sample as published in literature.

	SN 2018hti	LSQ14bdq	SN 2015bn	SN 2006oz	DES14X3taz
$Z/Z_{\odot}$	**0.3**	–	0.2 (Nicholl et al. 2016)	0.5 (Leloudas et al. 2012)	–
SFR [$M_{\odot}$ yr^{-1}]	**0.3**	<0.05 (Chen et al. 2017a)	0.04 (Nicholl et al. 2016)	0.17 (Leloudas et al. 2012)	0.16 (Smith et al. 2016)

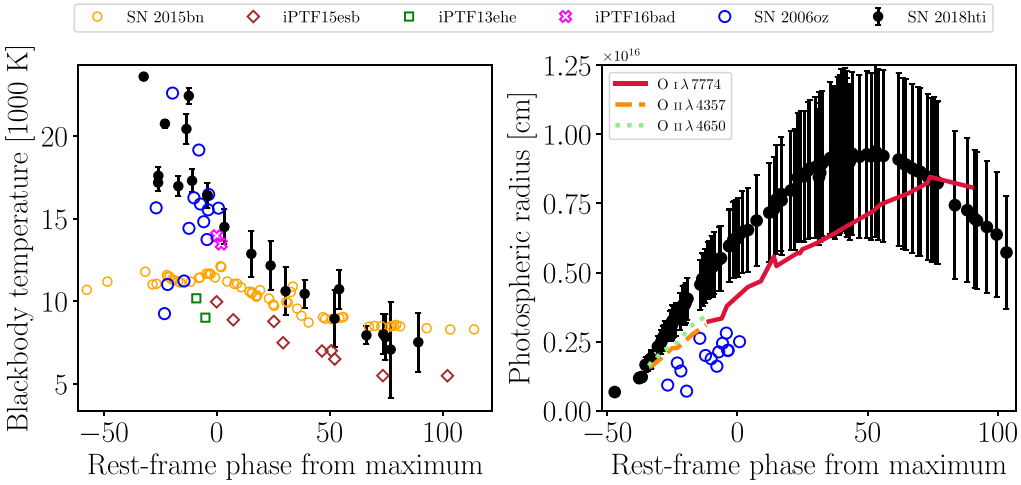

Figure 8. Left-hand panel: the blackbody temperatures of SN 2018hti (black filled dots). The blackbody temperature evolution of SN 2015bn (orange empty dots, Nicholl et al. 2016), SN 2006oz (blue empty dots, Leloudas et al. 2012), iPTF13ehe (green empty squares, Yan et al. 2015, 2017b), iPTF15esb (brown empty diamonds, Yan et al. 2017b), and iPTF16bad (magenta empty crosses, Yan et al. 2017b) are also shown for comparison. Right-hand panel: the evolution of the photospheric radius of SN 2018hti (black dots) compared with SN 2006oz. For comparison we also plot the radius obtained from the photospheric-velocity measurements performed on the spectra for the O I (red solid line) and the O II absorptions (λ 4357, orange dashed line, λ 4650, green dotted line).

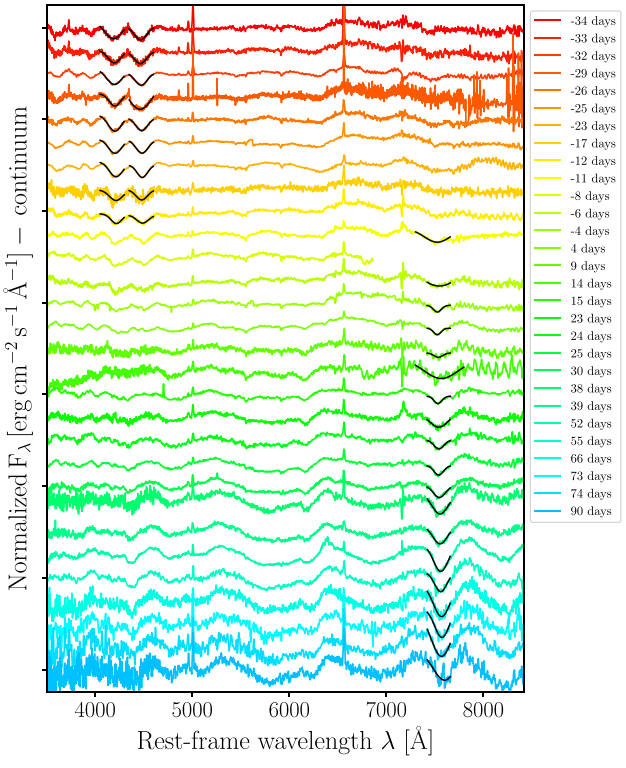

Figure 9. Normalized and continuum-subtracted spectra of SN 2018hti. A Gaussian curve (black solid line) is fitted to the absorption minima of the O II λλ 4357,4650 and the O I λ 7774 features. For the epochs in which more than one spectrum is available, we chose the spectrum with the greatest signal-to-noise ratio.

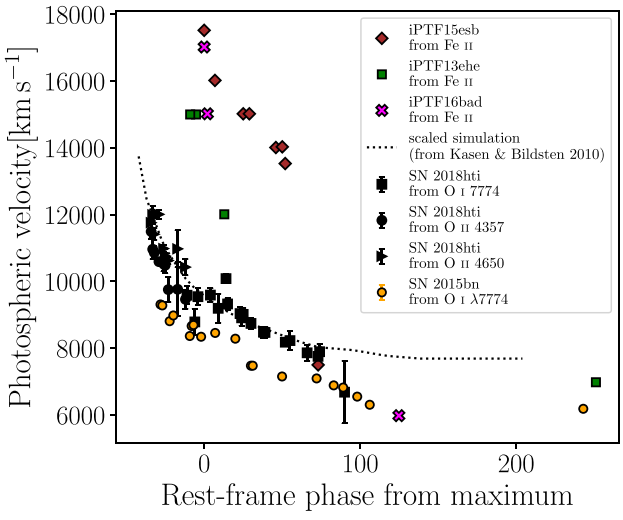

Figure 10. Photospheric velocities of SN 2018hti deduced from the absorption minima of O II λλ 4357,4650 (black dots and triangles) and O I λ 7774 (black squares) P-Cygni profiles (see the text). The evolution of the photospheric velocity of SN 2015bn (deduced by the O I, data taken from Nicholl et al. 2016, yellow dots), iPTF13ehe (green squares), iPTF15esb (brown diamonds), and iPTF16bad (magenta crosses) (deduced by the Fe II, Yan et al. 2017b) are shown for comparison. We also compared the photospheric velocity of SN 2018hti with the prediction of Kasen & Bildsten (2010) for a magnetar-powered SN (black dotted line, see the text).

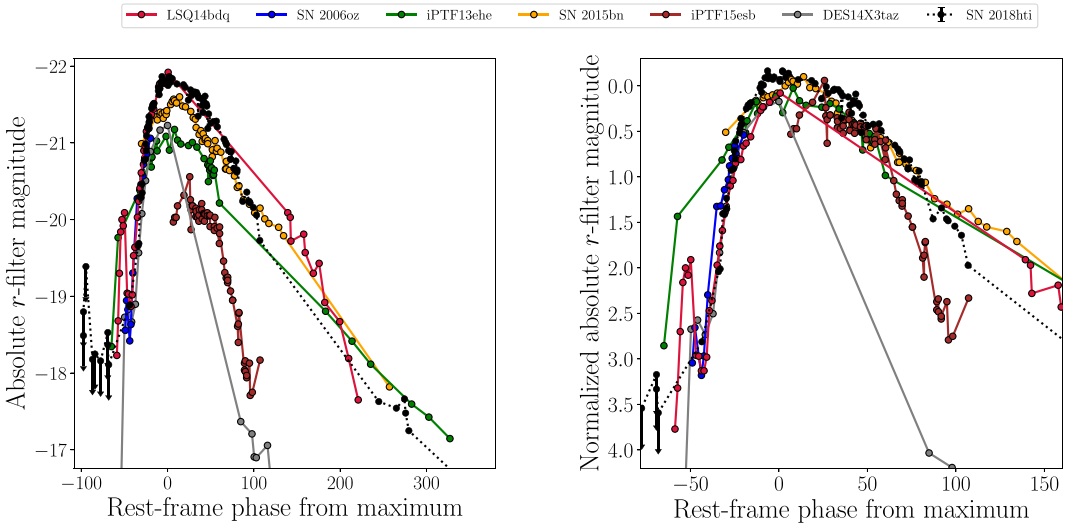

Figure 11. Left-hand panel: comparison of the *r*-filter absolute magnitude LC of SN 2018hti with those of LSQ14bdq (red dots), SN 2006oz (blue dots), iPTF13ehe (green dots), SN 2015bn (yellow dots), iPTF15esb (brown dots), and DES14X3taz (grey dots). Right-hand panel: same as the left-hand panel, but with the LCs normalized to maximum luminosity. Absolute magnitudes were corrected for Galactic extinction as in Section 2 and calculated with the assumed cosmology in this work. Where *K*-correction values were not available, we assume a constant *K*-correction $2.5\log(1+z)$.

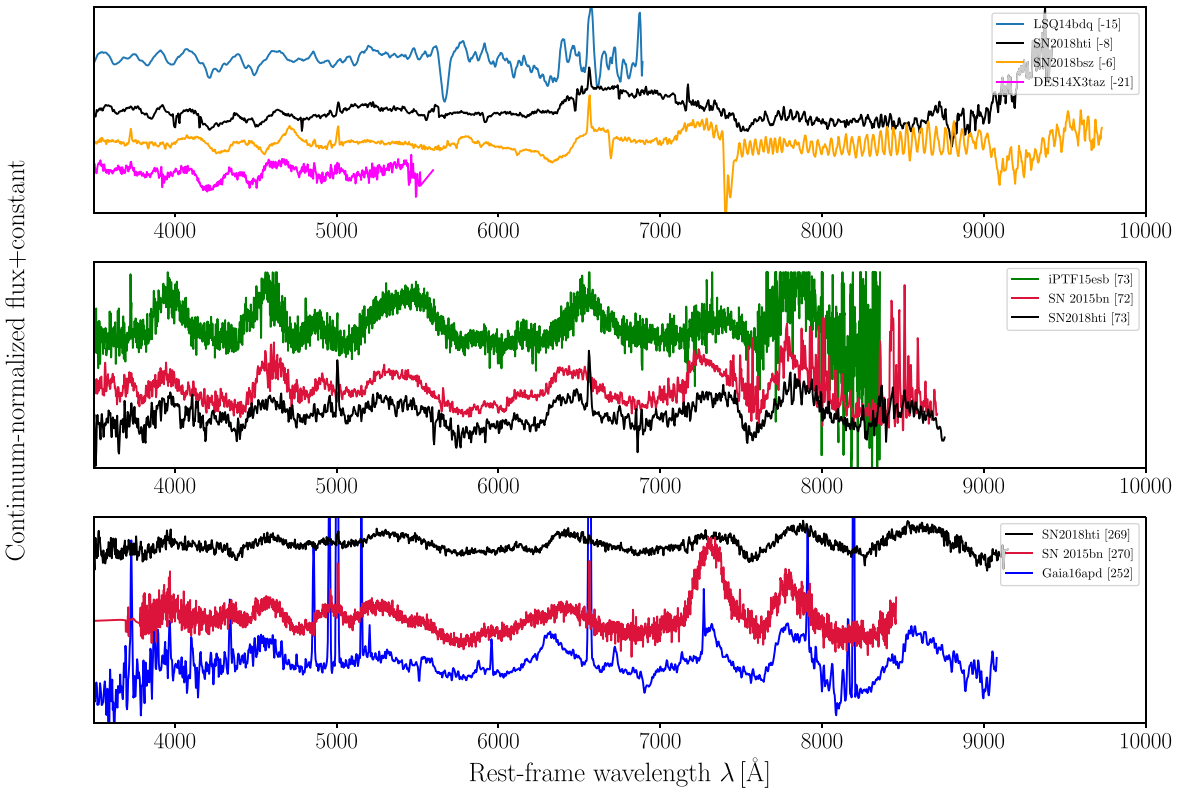

Figure 12. Comparisons of three spectra of SN 2018hti at different phases with respect to maximum luminosity (the rest-frame phase from maximum luminosity is indicated among square brackets in the legend). Upper panel: comparison among SN 2018hti (8 d before maximum, black line), SN 2018bsz (13 d before maximum, Anderson et al. 2018), LSQ14bdq (15 d before maximum, light blue line, see Nicholl et al. 2015b), and DES14X3taz (21 rest-frame days before maximum, magenta line, Smith et al. 2016). Middle panel: comparison among SN 2018hti (73 rest-frame days after maximum, black line), SN 2015bn (72 rest-frame days after maximum, red line), and iPTF15esb (73 rest-frame days from maximum, green line, see Yan et al. 2017b). Lower panel: comparison between SN 2018hti (269 rest-frame days after maximum, black line), SN 2015bn (270 rest-frame days after maximum, red line, see Nicholl et al. 2016), and Gaia16apd (252 rest-frame days after maximum, blue line, Kangas et al. 2017). For a better visualization, the spectrum of LSQ14bdq was smoothed with a Savitzki-Golay filter due to its lower signal-to-noise ratio. The spectra of iPTF15esb, 2018bsz, LSQ14bdq, SN 2015bn, and of Gaia16apd were obtained via WISEREP.

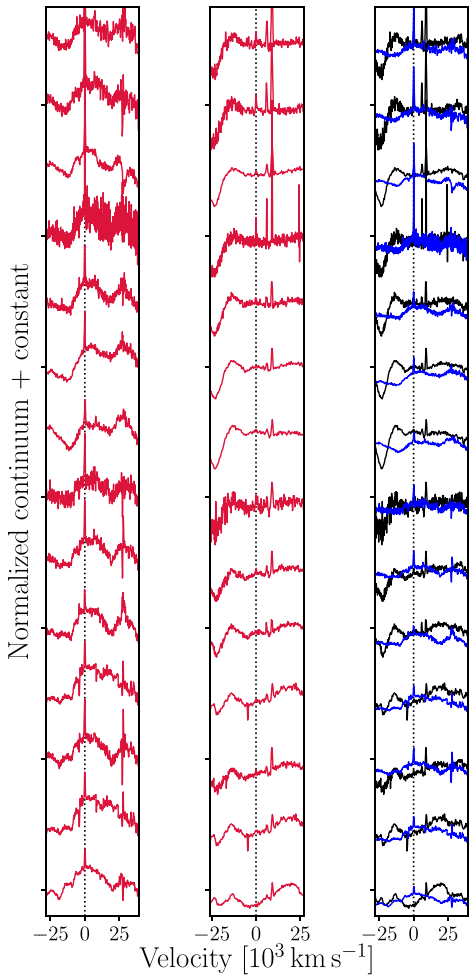

Figure 13. Left-hand panel: a close-up of the H α region in the early spectral evolution of SN 2018hti (red solid lines). Central panel: same as in the left-hand panel, but for the H β region. Right-hand panel: overlap of the H α (blue solid lines) and H β (black solid lines) regions, where the H α region was superposed on that of H β. The dotted vertical black lines mark the rest-frame wavelength of H β (middle panel) and of H α (left- and right-hand panel). The rest-frame phases of the spectra are labelled on the right side of the right-hand panel.

in SLSNe I (see Section 4.5.3) as a guide for the interpretation of the pseudo-nebular spectrum of SN 2018hti. This allows us to constrain the mass of the progenitor of SN 2018hti.

4.5.1 The early boxy feature

The flat-topped line profile of the emission feature at ∼6500 Å could be suitably explained by emission inside an expanding shell of matter (Weiler 2003; Jerkstrand 2017).The identification of this feature is not straightforward, and could be attributed either to H α or to C II λ 6580. To investigate this line identification, we superimpose on top of the boxy feature the line profiles of the possible H β (where a tiny bump is present, see Fig. 13) and of C II λ 9234 (see Fig. 14). The comparison between the H α and H β spectral regions is arduous because the H β region is also potentially contaminated by other spectral features (such as O II and Fe II). On the other hand, the boxy line is well reproduced by the C II λ 9234 feature in the IRTF+SpeX spectrum, suggesting that their flat profiles stem from the same matter

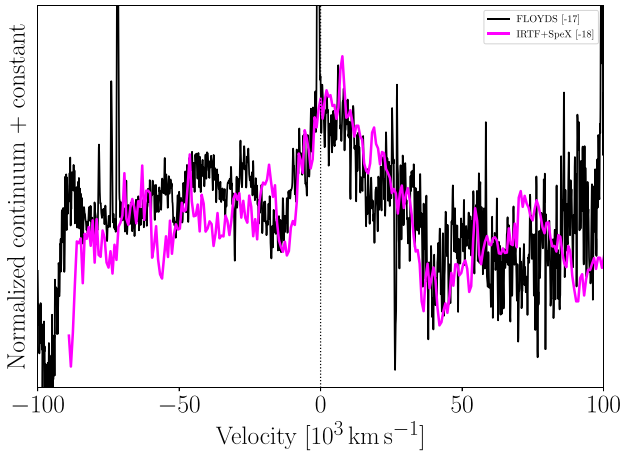

Figure 14. Comparison between the continuum-normalized FLOYDS (black line) and IRTF+SpeX (magenta line) spectra of SN 2018hti at comparable phases. The optical and the NIR spectra are plotted in velocity coordinates with respect to $\lambda = 6580$ Å and $\lambda = 9234$ Å, respectively.

shell and thus favouring a C II λ 6580 identification. Detailed radiative transfer calculations (e.g. Dessart et al. 2012; Dessart 2019) actually predict the presence of the C II λ 6580 feature in the SLSNe I spectra, but do not predict the boxy shape for the C II λ 6580. This suggests that the models may need to more carefully account for dynamical effects such as the formation of a thick shell, which is expected from both from magnetar and CSM interaction scenario.

4.5.2 Light curves fits with MOSFIT

MOSFIT includes a number of models for different kinds of astronomical transients. In particular, those suitable for the SLSNe I are the CSM (CSM interaction powered), CSMNI (CSM interaction $+^{56}$Ni-decay powered), the SLSN and the MAGNETAR (two implementations of the magnetar powered case, see later), and the MAGNI (magnetar$+^{56}$Ni-decay powered) models. We chose the SLSN and the CSM modules to fit the photometry of SN 2018hti, which, respectively, exploit the models introduced by Inserra et al. (2013) and Chatzopoulos, Wheeler & Vinko (2012). Since MOSFIT takes as input the multiband LCs, it has to rebuild the pseudo-bolometric luminosities once an SED model has been assumed. We chose the SLSN model since it accounts for the UV blanketing assuming an absorbed-blackbody model for the SED computation. We excluded the $W1$, $W2$ magnitudes from the fit procedure since the MIR part of the SED could deviate from a single blackbody component at epochs which are not covered by our photometric data set.

Also, the SLSN model includes constraints ensuring the energy conservation and that the ejecta do not become optically thin before 100 d after maximum, as not to contradict the late spectroscopic observations of the SLSNe (see section 3.8 in Nicholl et al. 2017b). The results of the fit procedures are shown in Figs 15 and 16 and the corner plots are shown in Figs S1 and S2 (available as online supplementary material). The SLSN fit supports a magnetar engine with a polar magnetic field of $\sim 1.3 \times 10^{13}$ G and an initial period of ~ 1.8 ms, for an ejecta mass $M_{\rm ejecta} \approx 5.3\,{\rm M}_{\odot}$, opacity $\kappa \approx 0.1\,{\rm cm^2\,g^{-1}}$, gamma-ray opacity $\kappa_{\gamma} \approx 0.02\,{\rm cm^2\,g^{-1}}$, an average ejecta velocity $v_{\rm ej} \approx 8500\,{\rm km\,s^{-1}}$, and a temperature floor $T_{\rm min} \approx 9300 \pm 250$ K. This corresponds to a kinetic energy $E_{\rm kin} = 3.7 \times 10^{51}$ erg. These results are absolutely reasonable for what is expected by the magnetar scenario for SLSNe I (e.g. Nicholl

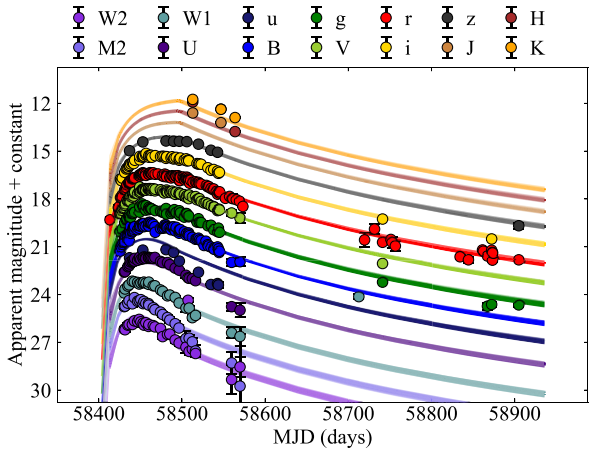

Figure 15. Best-fitting MOSFIT synthetic LCs to the multiband photometry of SN 2018hti obtained with the SLSN model.

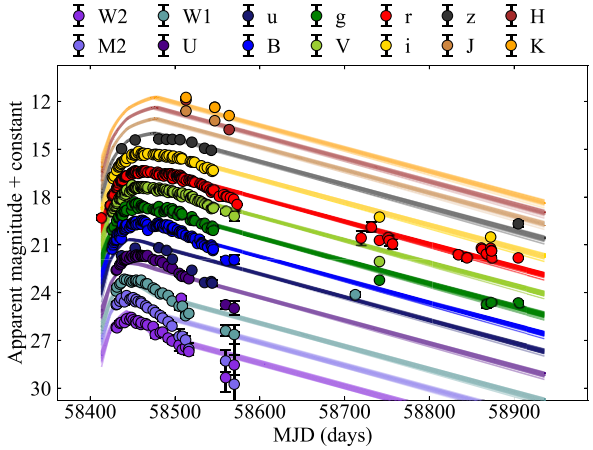

Figure 16. Same as in Fig. 15, but for the CSM model.

et al. 2017b) and are in perfect agreement with the estimates of Lin et al. (2020a). Except for the ejecta mass, the best-fitting parameters for the magnetar case are quite different from those assumed in the calculations of Kasen & Bildsten (2010). This difference could possibly explain the need of the scaling factor 1.37 that we used in Section 4.3 to match the predicted photospheric velocity with the observed one. Moreover, the value of the kinetic energies required by both interpretations largely overcomes the maximum explosion energy that can be provided by a neutrino-driven mechanism during the core collapse (Soker & Gilkis 2017; Kaplan & Soker 2020). This energy budget might require the contribution of jets in the explosion of SN 2018hti. However, its negligible polarization degree (Lee 2019) suggests that its explosion was nearly spherical, thus making this hypothesis less likely.

The CSM fit of SN 2018hti instead requires the interaction of the SN ejecta with a mass of $\sim 8.3\,M_\odot$ and average velocity $v_{ej} \approx 1.1 \times 10^4\,km\,s^{-1}$ with a CSM mass $M_{CSM} \approx 10.5\,M_\odot$ and average density $\rho \approx 4.1 \times 10^{-13}\,g\,cm^{-3}$. This corresponds to a kinetic energy $E_{kin} = 1.1 \times 10^{52}$ erg. Also, for this model the predicted temperature floor reached by SN 2018hti is $T_{min} \approx 9500 \pm 180$ K. Both the predictions of T_{min} can be considered in agreement with what was deduced in Section 4.2. The best-fitting slope of the CSM density profile $s \sim 0.2$ seemingly favours a shell-like CSM with nearly constant density (Chatzopoulos et al. 2013). The CSM interaction scenario may be disfavoured because of the absence of narrow/multicomponent features in the spectra (typical e.g. of SNe IIn) and because there was no significant detection in X-ray (see Section 2). However, these arguments cannot rule out the CSM-interaction scenario for SN 2018hti if the CSM is highly asymmetric, e.g. if it has a disc-like geometry. In fact, if the CSM is not seen perfectly edge on, the optically thick ejecta may form a photosphere outside the CSM so that the ejecta CSM interaction takes place underneath it and the X-ray, UV photons can be reprocessed by further radiation–matter interactions (as it was proposed by Andrews & Smith 2018, for the peculiar SN II iPTF14hls).

4.5.3 *Interpretation of the nebular spectrum*

The nebular spectrum of SN 2018hti taken 269 rest-frame days after maximum light was interpreted with SUMO modelling (Jerkstrand et al. 2017).The best-matching SUMO models are built with a C-burning composition, $M_{ejecta} = 30\,M_\odot$, a filling factor $f = 0.001$, an energy deposition $E_{dep} = 10^{42}\,erg\,s^{-1}$ and a pure-O abundance $M_{ejecta} = 10\,M_\odot$, $f = 0.1$, $E_{dep} = 2 \times 10^{42}\,erg\,s^{-1}$. In the following text, we will refer to them as C30 and O10, respectively. They are shown in Fig. 17 with the pseudo-nebular spectrum of SN 2018hti. In particular, O10 better reproduces the bluer region of the spectrum (until ∼5200 Å, see Fig. 17), whereas C30 better matches the redder region. Also, the best-matching spectra permit identification of other broad features in the spectrum, such as [O III] λλ 4959, 5007, Mg I λ 5180+[Fe II] λ 5250, and [O I] λ 5577. We estimated the progenitor mass of SN 2018hti by measuring the flux emitted within the O I λ 7774 emission feature predicted by C30 using equations (7) and (8) of Jerkstrand et al. (2017). The choice of C30 is motivated by the fact that it better describes the Oxygen features in the spectrum, as the [O I] λλ 6300, 6364 and [O I] λ 5577 features. The flux integrated within the O I λ 7774 feature gives $L_{7774} = 2.25 \times 10^{40}\,erg\,s^{-1}$. Hence, we assumed $f = 0.001$, the Oxygen mean molecular weight $\bar{A} = 16$, an electron fraction $x_e = 0.1$ (Jerkstrand et al. 2017, see their section 4.2.1), a maximum expansion velocity $V = 8\,000\,km\,s^{-1}$ (we adopted for V a value consistent with the velocity plateau at late times, see Fig. 10), and a recombination coefficient $\alpha^{eff}(T) = 2 \times 10^{-13}\,cm^3\,s^{-1}$. Solving equation (7) of Jerkstrand et al. (2017) for the electron density n_e, this gives $n_e \sim 1.28 \times 10^9\,cm^{-3}$. Using this value in equation (8) in Jerkstrand et al. (2017), the O-zone mass is estimated to be $M_{O-zone} \approx 6.2\,M_\odot$, which according to more recent models of stellar evolution of a single star corresponds to a progenitor mass $M_{ZAMS} \approx 40\,M_\odot$ (Jerkstrand et al. 2017). Similar consideration can be made for the O10 solution (corresponding to $f = 0.1$ and $x_e \approx 0.5$), which predicts a O-zone mass $M_{O-zone} \approx 10\,M_\odot$ (for this solution we require $V \lesssim 7\,000\,km\,s^{-1}$ in order not to obtain $M_{O\text{-zone}} > M_{ejecta}$). In the latter case, the ejecta is expected to be much Mg-poorer compared to the C30 case. Another reason to favour the C30 model lies in its ejecta clump density. In fact, C30 is 300 times denser than O10.[13] This could be also the reason why no strong [O I]λ 6300 and [Ca II] + [O II] λ 7300 emission is seen in the nebular spectrum, as it would emerge for higher density models.

Finally, in Table 3 we summarized the ejecta-mass estimates obtained with the MOSFIT fits and the SUMO nebular modelling. The SUMO O10 solution apparently favours the CSM model since the

[13] The factor 300 comes from $(30\,M_\odot/f_{C30})/(10\,M_\odot/f_{O10}) = 300$, where $f_{C30} = 0.001$ and $f_{O10} = 0.1$ are the clumping factors for the models C30 and O10, respectively.

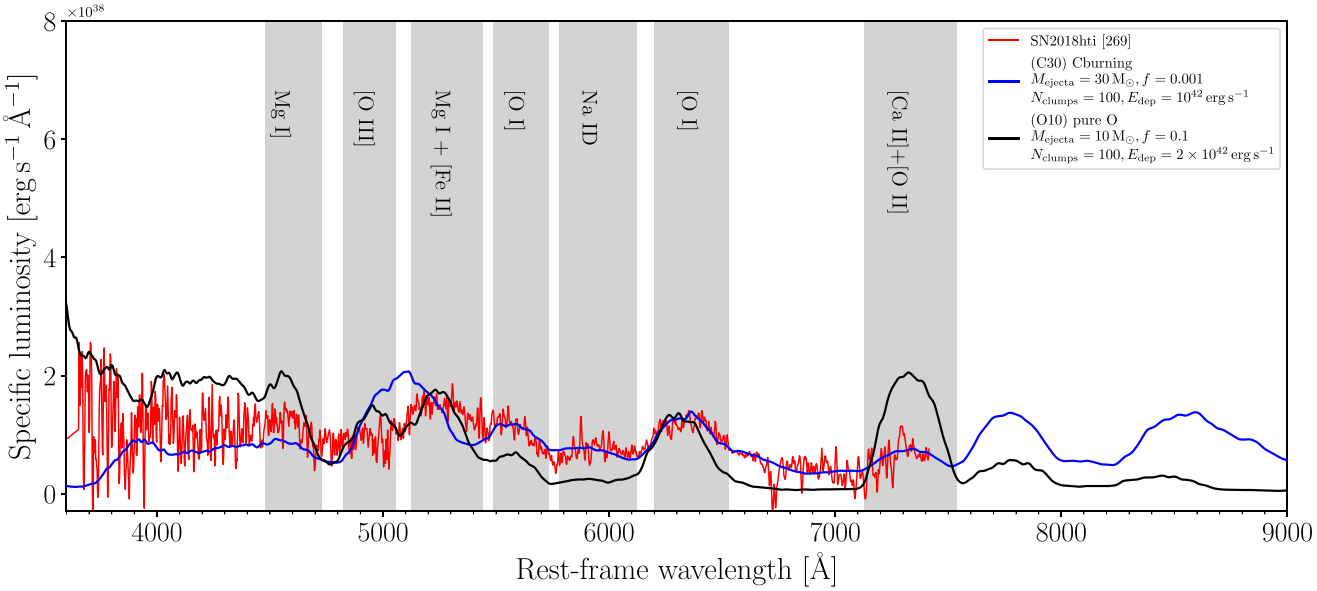

Figure 17. Comparison of the GTC+OSIRIS nebular spectrum (red line) with two outputs of the SUMO numerical code (see the text) for a full C-ashes model (blue line) and a pure-O composition (black line).

Table 3. Comparison of the ejecta masses of the best-matching SUMO solutions with MOSFIT best-fitting parameters.

	Ejecta mass [$M_\odot$]
SUMO	10–30
MOSFIT CSM	8.32
MOSFIT SLSN	5.25

ejecta mass used by O10 nearly reproduces that one estimated by the MOSFIT CSM fit, whereas the MOSFIT SLSN fit predicts an ejecta mass which is pretty lower than what is suggested by the SUMO solutions. However, we warn the reader that the (single-zone) SUMO solutions are computed for a phase of 400 d post-explosion, which is not the case for the pseudo-nebular spectrum of SN 2018hti. Hence, the density in the model is by a factor $(400/270)^3 \simeq 3.3$ lower than the corresponding case at 270 d. This biases a direct constrain on the ejecta density and mass. In addition, it is hard to believe that in the case of SN 2018hti the CSM interaction is acting as its major power source even if we interpret the modest C II boxy feature as a signature of the interaction with a CSM dense shell. According to the MOSFIT CSM fit, the predicted CSM mass is $\sim$10.5 $M_\odot$. We expect that the interaction with a similar amount of mass of CSM would cause strong spectral emissions as in the case of the Type IIn SN 2008iy (Chugai 2021) and SN 2010jl (Ofek et al. 2014). However, as we mentioned earlier, a disc-like and dense CSM can hide the spectral signatures of CSM-interaction. Based on this considerations, we argue that the mechanism powering SN 2018hti could be either the spin-down radiation from a millisecond magnetar with $B_p \sim 1.3 \times 10^{13}$ G and $P_{spin} \sim 1.8$ ms or the (buried) interaction of the ejecta with $\sim$10 $M_\odot$ of a disc-like CSM.

5 CONCLUSIONS

In this work, we have presented the UV/optical/NIR photometry and the NIR/optical spectroscopy of the SLSN I SN 2018hti. It slowly rose for $\sim$50 d towards a peak absolute magnitude of -21.7 mag in the r band. Alongside this slow rise and extremely high luminosity, the presence of the prominent O II absorptions in the pre-maximum/maximum spectra identifies this object as a (slow-evolving) SLSN I. In the Hα region, the early spectra show a flat-topped feature which we interpret as Hα. C-rich SLSNe I spectra are predicted by magnetar- and a pair-instability-driven radiative transfer calculations (Dessart et al. 2012; Dessart 2019), but the boxy profile suggests that the feature could originate from the shock-mediated interaction of the SN ejecta with a surrounding CSM. In addition, metallicity measurements via the host narrow emission lines are aligned with the low-metallicity paradigm of SLSNe I. Finally, we estimated the physical parameters of the explosion, both in the magnetar and in the CSM-interaction scenarios, fitting synthetic LCs to the multicolour photometry of SN 2018hti with the MOSFIT tool. The model fits suggest that either interaction of a 8 $M_\odot$ SN ejecta with $\sim$10 $M_\odot$ of CSM or the spin-down radiation of a $B \sim 1.3 \times 10^{13}$ G, $P_{spin} \sim 1.8$ ms magnetar could be the major power source for SN 2018hti.

We interpret the pseudo-nebular spectrum of SN 2018hti with synthetic spectra published by Jerkstrand et al. (2017) for an SN Ic. We concluded that, assuming a single-star progenitor scenario for SN 2018hti, the progenitor ZAMS mass was of $\sim$40 $M_\odot$. These findings help to unravel the origin of the complexities that often appear in SLSNe-I LCs (e.g. Inserra et al. 2017), finding a reasonable explanation in CSM-ejecta interaction. This sheds light on the nature of SLSNe I progenitors.

The advent of the new-generation, wide-field surveys such as the Legacy Survey of Space and Time at the Vera Rubin Observatory will contribute to broaden our knowledge about the SLSN astrophysics (Villar, Nicholl & Berger 2018).

ACKNOWLEDGEMENTS

We thank the anonymous referee for her/his valuable comments which improved the present work. AF acknowledges Stephen Smarrt, Marica Branchesi, Noam Soker, and Morgan Fraser for their sug-

gestions and for interesting discussions. This work is based on observations made with the Nordic Optical Telescope, owned in collaboration by the University of Turku and Aarhus University, and operated jointly by Aarhus University, the University of Turku and the University of Oslo, representing Denmark, Finland and Norway, the University of Iceland and Stockholm University at the Observatorio del Roque de los Muchachos, La Palma, Spain, of the Instituto de Astrofisica de Canarias. The data presented here were obtained in part with ALFOSC, which is provided by the Instituto de Astrofisica de Andalucia (IAA) under a joint agreement with the University of Copenhagen and NOT. Based on observations collected at Copernico and Schmidt telescopes (Asiago, Italy) of the INAF - Osservatorio Astronomico di Padova. MG is supported by the EU Horizon 2020 research and innovation programme under grant agreement No 101004719. MS acknowledges the Infrared Telescope Facility, which is operated by the University of Hawaii under contract 80HQTR19D0030 with the National Aeronautics and Space Administration. NER acknowledges support from MIUR, PRIN 2017 (grant 20179ZF5KS). TMB was funded by the CONICYT PFCHA / DOCTORADOBECAS CHILE/2017-72180113. AJ acknowledges funding from the European Research Council (ERC) under the European Union's Horizon 2020 Research and Innovation Program (ERC Starting Grant. AR acknowledges support from ANID BECAS/DOCTORADO NACIONAL 21202412. Y-Z Cai is funded by China Postdoctoral Science Foundation (grant no. 2021M691821). T-WC acknowledges the EU Funding under Marie Skłodowska-Curie grant H2020-MSCA-IF-2018-842471. KM is funded by the EU H2020 ERC grant no. 758638. GP is supported by ANID - Millennium Science Initiative - ICN12_009. We thank the staff at the different observatories for performing the observations. Based on observations collected at the European Organisation for Astronomical Research in the Southern Hemisphere, Chile, as part of ePESSTO+ (the advanced Public ESO Spectroscopic Survey for Transient Objects). ePESSTO+ observations were obtained under ESO program id 199.D-0143 (PI: Inserra). Based on observations made with the Gran Telescopio Canarias (GTC), installed in the Spanish Observatorio del Roque de los Muchachos of the Instituto de Astrofísica de Canarias, in the island of La Palma. This work uses observations from the Las Cumbres Observatory network. The LCO team is supported by NSF grants AST-1911225 and AST-1911151.

DATA AVAILABILITY STATEMENT

The data presented in this paper and listed in Appendix A are available in the online supplementary material. The spectra will be made public via WISEREP.

REFERENCES

(HEASARC) N. H. E. A. S. A. R. C., 2014, Astrophysics Source Code Library, record ascl:1408.004
Agnoletto I. et al., 2009, ApJ, 691, 1348
Anderson J. P. et al., 2018, A&A, 620, A67
Anderson J. P., 2019, A&A, 628, A7
Andrews J. E., Smith N., 2018, MNRAS, 477, 74
Angus C. R. et al., 2019, MNRAS, 487, 2215
Asplund M., Grevesse N., Sauval A. J., Scott P., 2009, ARA&A, 47, 481
Becker A., 2015, Astrophysics Source Code Library, record ascl:1504.004
Bhirombhakdi K., Chornock R., Miller A. A., Filippenko A. V., Cenko S. B., Smith N., 2019, MNRAS, 488, 3783
Bianco F. B., Modjaz M., Oh S. M., Fierroz D., Liu Y. Q., Kewley L., Graur O., 2016, Astron. Comput., 16, 54
Blanchard P. K., Nicholl M., Berger E., Chornock R., Milisavljevic D., Margutti R., Gomez S., 2019, ApJ, 872, 90
Brown T. M. et al., 2013, PASP, 125, 1031
Burke J., Hiramatsu D., Arcavi I., Howell D. A., Mccully C., Valenti S., 2018, Transient Name Server Classification Report, 2018–1719, 1
Cappellaro E., 2014, snoopy: a package for SN photometry, Available at: http://sngroup.oapd.inaf.it/snoopy.html
Cardelli J. A., Clayton G. C., Mathis J. S., 1988, ApJ, 329, L33
Cardelli J. A., Clayton G. C., Mathis J. S., 1989, ApJ, 345, 245
Cepa J. et al., 2000, in Iye M., Moorwood A. F., eds, Proc. SPIE Conf. Ser. Vol. 4008, Optical and IR Telescope Instrumentation and Detectors. SPIE, Bellingham, p. 623
Chambers K. C. et al., 2016, preprint (arXiv:1612.05560)
Chatzopoulos E., Wheeler J. C., Vinko J., 2012, ApJ, 746, 121
Chatzopoulos E., Wheeler J. C., Vinko J., Horvath Z. L., Nagy A., 2013, ApJ, 773, 76
Chen T.-W. et al., 2013, ApJ, 763, L28
Chen K.-J., Woosley S. E., Sukhbold T., 2016, ApJ, 832, 73
Chen T.-W., Smartt S. J., Yates R. M., Nicholl M., Krühler T., Schady P., Dennefeld M., Inserra C., 2017a, MNRAS, 470, 3566
Chen T. W. et al., 2015, MNRAS, 452, 1567
Chen T. W. et al., 2017b, A&A, 602, A9
Chevalier R. A., Fransson C., 2003, Supernova Interaction with a Circumstellar Medium. Springer Berlin Heidelberg, Berlin, Heidelberg, p. 171
Chevalier R. A., Irwin C. M., 2011, ApJ, 729, L6
Chonis T. S., Gaskell C. M., 2008, AJ, 135, 264
Chugai N. N., 2021, MNRAS, 508, 6023
Conley A. et al., 2006, AJ, 132, 1707
Cushing M. C., Vacca W. D., Rayner J. T., 2004, PASP, 116, 362
De Cia A. et al., 2018, ApJ, 860, 100
Denicoló G., Terlevich R., Terlevich E., 2002, MNRAS, 330, 69
Dessart L., 2019, A&A, 621, A141
Dessart L., Hillier D. J., Waldman R., Livne E., Blondin S., 2012, MNRAS, 426, L76
Dessart L., Hillier D. J., Woosley S., Livne E., Waldman R., Yoon S.-C., Langer N., 2015, MNRAS, 453, 2189
Elias-Rosa N. et al., 2006, MNRAS, 369, 1880
Fiore A. et al., 2021, MNRAS, 502, 2120
Gal-Yam A., 2012, Science, 337, 927
Gal-Yam A., 2019a, ARA&A, 57, 305
Gal-Yam A., 2019b, ApJ, 882, 102
Gal-Yam A., Yaron O., Pastorello A., Taubenberger S., Fraser M., Perley D., 2021, Transient Name Server AstroNote, 76, 1
Gehrels N. et al., 2004, ApJ, 611, 1005
Ginzburg S., Balberg S., 2012, ApJ, 757, 178
Gomez S., Berger E., Hosseinzadeh G., Blanchard P. K., Nicholl M., Villar V. A., 2021, ApJ, 913, 143
Groves B., Brinchmann J., Walcher C. J., 2012, MNRAS, 419, 1402
Guillochon J., Nicholl M., Villar V. A., Mockler B., Narayan G., Mandel K. S., Berger E., Williams P. K. G., 2017, Astrophysics Source Code Library, record ascl:1710.006
Guillochon J., Nicholl M., Villar V. A., Mockler B., Narayan G., Mandel K. S., Berger E., Williams P. K. G., 2018, ApJS, 236, 6
Harris J., Zaritsky D., 2009, AJ, 138, 1243
Harutyunyan A. H. et al., 2008, A&A, 488, 383
Heger A., Woosley S. E., 2002, ApJ, 567, 532
Holmbo S. et al., 2019, The Astronomer's Telegram, 12661, 1
Hosseinzadeh G., Berger E., Metzger B. D., Gomez S., Nicholl M., Blanchard P., 2021, preprint (arXiv:2109.09743)
Howell D. A., 2017, Superluminous Supernovae. Springer International Publishing, Cham, p. 431
Inserra C. et al., 2013, ApJ, 770, 128
Inserra C. et al., 2017, MNRAS, 468, 4642
Inserra C., 2019, Nat. Astron., 3, 697
Jeffery D. J., Branch D., 1990, in Wheeler J. C., Piran T., Weinberg S., eds, Jerusalem Winter School for Theoretical Physics Vol. 6, Supernovae. World Scientific Publishing Co., Singapore, p. 149
Jerkstrand A. et al., 2017, ApJ, 835, 13

Jerkstrand A., 2017, Spectra of Supernovae in the Nebular Phase. Springer International Publishing, Cham, p. 795
Kangas T. et al., 2017, MNRAS, 469, 1246
Kaplan N., Soker N., 2020, MNRAS, 492, 3013
Kasen D., Bildsten L., 2010, ApJ, 717, 245
Kasen D., Woosley S. E., Heger A., 2011, ApJ, 734, 102
Kennicutt Robert C. J., 1998, ARA&A, 36, 189
Kewley L. J., Dopita M. A., 2002, ApJS, 142, 35
Kewley L. J., Ellison S. L., 2008, ApJ, 681, 1183
Khetan N. et al., 2021, A&A, 647, A72
Könyves-Tóth R., Vinkó J., 2021, ApJ, 909, 24
Lee C.-H., 2019, ApJ, 875, 121
Leloudas G. et al., 2012, A&A, 541, A129
Leloudas G. et al., 2015, MNRAS, 449, 917
Lin W. L. et al., 2020a, MNRAS, 497, 318
Lin W. L., Wang X. F., Wang L. J., Dai Z. G., 2020b, ApJ, 903, L24
Lunnan R. et al., 2014, ApJ, 787, 138
Lunnan R. et al., 2018a, Nat. Astron., 2, 887
Lunnan R. et al., 2018b, ApJ, 852, 81
Lunnan R. et al., 2020, ApJ, 901, 61
Maiolino R. et al., 2008, A&A, 488, 463
Margalit B., Metzger B. D., Thompson T. A., Nicholl M., Sukhbold T., 2018, MNRAS, 475, 2659
Marino R. A. et al., 2013, A&A, 559, A114
Mattila S. et al., 2016, The Astronomer's Telegram, 8992, 1
Mazzali P. A., Sullivan M., Pian E., Greiner J., Kann D. A., 2016, MNRAS, 458, 3455
McGaugh S. S., 1991, ApJ, 380, 140
Metzger B. D., Vurm I., Hascoët R., Beloborodov A. M., 2014, MNRAS, 437, 703
Minkowski R., 1941, PASP, 53, 224
Modjaz M., Gutiérrez C. P., Arcavi I., 2019, Nat. Astron., 3, 717
Moriya T. J., Tominaga N., 2012, ApJ, 747, 118
Moriya T. J., Sorokina E. I., Chevalier R. A., 2018, Space Sci. Rev., 214, 59
Müller T., Prieto J. L., Pejcha O., Clocchiatti A., 2017, ApJ, 841, 127
Nadyozhin D. K., 1994, ApJS, 92, 527
Nicholl M. et al., 2014, MNRAS, 444, 2096
Nicholl M. et al., 2015a, MNRAS, 452, 3869
Nicholl M. et al., 2015b, ApJ, 807, L18
Nicholl M. et al., 2016, ApJ, 826, 39
Nicholl M. et al., 2020, Nat. Astron., 4, 893
Nicholl M., Berger E., Margutti R., Blanchard P. K., Milisavljevic D., Challis P., Metzger B. D., Chornock R., 2017a, ApJ, 835, L8
Nicholl M., Guillochon J., Berger E., 2017b, ApJ, 850, 55
Nicholl M., Berger E., Blanchard P. K., Gomez S., Chornock R., 2019, ApJ, 871, 102
Ofek E. O. et al., 2014, ApJ, 781, 42
Pagel B. E. J., Edmunds M. G., Blackwell D. E., Chun M. S., Smith G., 1979, MNRAS, 189, 95
Parrag E. et al., 2021, MNRAS, 506, 4819
Pastorello A. et al., 2010, ApJ, 724, L16
Pastorello A. et al., 2021, Transient Name Server Classification Report, 2021–511, 1
Perley D. A. et al., 2015, ApJ, 801, 102
Pignata G. et al., 2004, MNRAS, 355, 178
Planck Collaboration XIII, 2016, A&A, 594, A13
Prentice S. J. et al., 2019, MNRAS, 485, 1559
Quimby R. M. et al., 2011, Nature, 474, 487
Rayner J. T., Toomey D. W., Onaka P. M., Denault A. J., Stahlberger W. E., Vacca W. D., Cushing M. C., Wang S., 2003, PASP, 115, 362
Renzo M., Farmer R., Justham S., Götberg Y., de Mink S. E., Zapartas E., Marchant P., Smith N., 2020, A&A, 640, A56
Richardson D., Jenkins R. L. I., Wright J., Maddox L., 2014, AJ, 147, 118
Riess A. G. et al., 1999, AJ, 118, 2675
Riess A. G., Casertano S., Yuan W., Bowers J. B., Macri L., Zinn J. C., Scolnic D., 2021, ApJ, 908, L6
Roy R. et al., 2016, A&A, 596, A67
Schlafly E. F., Finkbeiner D. P., 2011, ApJ, 737, 103
Schulze S. et al., 2018, MNRAS, 473, 1258
Skrutskie M. F. et al., 2006, AJ, 131, 1163
Smartt S. J. et al., 2015, A&A, 579, A40
Smartt S. J., 2009, ARA&A, 47, 63
Smith N. et al., 2007, ApJ, 666, 1116
Smith N. et al., 2015, MNRAS, 449, 1876
Smith M. et al., 2016, ApJ, 818, L8
Smith N., 2017, Interacting Supernovae: Types IIn and Ibn. Springer International Publishing, Cham, p. 403
Smith N., McCray R., 2007, ApJ, 671, L17
Soderberg A. M. et al., 2008, Nature, 453, 469
Soker N., Gilkis A., 2017, ApJ, 851, 95
Stevance H. F., Eldridge J. J., 2021, MNRAS, 504, L51
Stritzinger M. et al., 2002, AJ, 124, 2100
Tonry J. et al., 2018b, Transient Name Server Discovery Report, 2018–1680, 1
Tonry J. L. et al., 2012, ApJ, 750, 99
Tonry J. L. et al., 2018a, ApJ, 867, 105
van Dokkum P. G., 2001, PASP, 113, 1420
Villar V. A., Nicholl M., Berger E., 2018, ApJ, 869, 166
Vurm I., Metzger B. D., 2021, ApJ, 917, 77
Wang S. Q., Wang L. J., Dai Z. G., Wu X. F., 2015, ApJ, 799, 107
Weiler K., 2003, Supernovae and Gamma-Ray Bursters. Lecture Notes in Physics Vol. 598. Springer, Berlin, Heidelberg
Woosley S. E., 2010, ApJ, 719, L204
Woosley S. E., 2017, ApJ, 836, 244
Woosley S. E., Blinnikov S., Heger A., 2007, Nature, 450, 390
Yan L. et al., 2015, ApJ, 814, 108
Yan L. et al., 2017a, ApJ, 840, 57
Yan L. et al., 2017b, ApJ, 848, 6
Yang Y. et al., 2020, ApJ, 902, 46
Yaron O., Gal-Yam A., 2012, PASP, 124, 668
Zaritsky D., Kennicutt Robert C. J., Huchra J. P., 1994, ApJ, 420, 87
Zou Y.-C., Cheng K. S., 2018, Publ. Astron. Soc. Aust., 35, 32

SUPPORTING INFORMATION

Supplementary data are available at *MNRAS* online.

Please note: Oxford University Press is not responsible for the content or functionality of any supporting materials supplied by the authors. Any queries (other than missing material) should be directed to the corresponding author for the article.

APPENDIX A: TABLES

Table A1. *uvw*1-, *uvm*2-, *uvw*2-filter observed (non *K*-corrected) aperture magnitudes (in AB system). Errors are in parentheses. The full table is available online as supplementary material..

MJD	r. f. phase [d]	*uvw*2	*uvm*2	*uvw*1	Instrument
58430.65	− 31.89	20.17(0.12)	19.76(0.14)	18.90(0.09)	*Swift*/UVOT
58431.56	− 31.03	20.21(0.12)	19.73(0.12)	18.65(0.08)	*Swift*/UVOT
58434.92	− 27.87	19.92(0.11)	19.54(0.12)	18.47(0.08)	*Swift*/UVOT
58436.44	− 26.44	19.88(0.11)	19.37(0.11)	18.39(0.08)	*Swift*/UVOT
–	–	–	–	–	–

Table A2. *u*-, *g*-, *r*-, *i*-, *z*-filter observed (non *K*-corrected, non S-corrected) magnitudes (in AB system). Errors are in parentheses. The full table is available online as supplementary material.

MJD	r. f. phase [d]	*u*	*g*	*r*	*i*	*z*	Instrument
58413.54	− 48.01	–	–	19.31(0.16)	–	–	ATLAS
58423.53	− 38.60	–	–	18.54(0.19)	–	–	ATLAS
58424.54	− 37.65	–	–	18.51(0.14)	–	–	ATLAS
58426.12	− 36.16	–	18.05(0.01)	17.90(0.01)	17.76(0.02)	–	LCO+Sinistro
–	–	–	–	–	–	–	

Table A3. *U*-, *B*-, *V*-observed (non *K*-corrected, non S-corrected) magnitudes (in AB system). The full table is available online as supplementary material.

MJD	r. f. phase [d]	*U*	*B*	*V*	Instrument
58426.12	− 36.16	–	18.37(0.01)	17.90(0.02)	LCO+Sinistro
58427.15	− 35.19	–	18.09(0.02)	17.87(0.01)	LCO+Sinistro
58428.31	− 34.1	–	17.95(0.02)	17.69(0.01)	LCO+Sinistro
58429.29	− 33.17	–	17.83(0.04)	17.56(0.01)	LCO+Sinistro
–	–	–	–	–	–

Table A4. *J*-, *H*-, K_s-observed (non *K*-corrected) magnitudes (in AB system). Errors are in parentheses.

MJD	r. f. phase [d]	*J*	*H*	K_s	Instrument
58512.96	45.56	15.60(0.01)	15.91(0.01)	16.75(0.01)	NOT+NOTCam
58546.87	77.51	16.21(0.02)	16.36(0.02)	17.37(0.03)	NOT+NOTCam
58563.85	93.50	–	17.77(0.04)	17.89(0.04)	NOT+NOTCam

Table A5. *W*1-, *W*2-observed (non *K*-corrected) magnitudes (in AB system). Errors are in parentheses.

MJD	r. f. phase [d]	*W*1	*W*2	Instrument
58507.39	40.04	17.95(0.07)	18.33(0.13)	WISE
58712.64	233.69	19.13(0.16)	$\gtrsim$18.61	WISE

Table A6. S-corrections for Schmidt and AFOSC filters (Asiago observatory). The full table is available online as supplementary material.

MJD	*B*	*g*	*V*	*r*	*i*
58430.25	− 0.02	0.01	0.018	0.113	0.053
58437.02	− 0.019	0.014	0.022	0.122	0.048
58437.14	− 0.017	0.014	0.019	0.127	0.06
58440.23	− 0.027	0.012	0.018	0.101	0.064
–	–	–	–	–	–

Table A7. S-corrections for Sinistro (LCO). The full table is available online as supplementary material.

MJD	*B*	*g*	*V*	*r*	*i*
58430.25	− 0.009	0.003	0.009	0.004	− 0.005
58437.02	− 0.008	0.004	0.003	0.007	− 0.002
58437.14	− 0.008	0.005	0.011	0.005	− 0.001
58440.23	− 0.009	0.004	0.009	− 0.007	− 0.0
–	–	–	–	–	–

Table A8. S-corrections for NOT filters. The full table is available online as supplementary material.

MJD	*B*	*g*	*V*	*r*	*i*
58430.25	− 0.013	0.001	0.008	0.011	− 0.008
58437.02	− 0.013	− 0.004	0.005	0.013	− 0.011
58437.14	− 0.014	− 0.002	0.011	0.015	− 0.013
58440.23	− 0.015	− 0.005	0.007	0.002	0.011
–	–	–	–	–	–

Table A9. S-corrections for *Swift*/UVOT. The full table is available online as supplementary material.

MJD	*B*	*V*
58430.25	− 0.017	0.009
58437.02	− 0.018	0.008
58437.14	− 0.017	0.019
58440.23	− 0.02	0.006
–	–	–

Table A10. Estimated uncertainties $\Delta S_{\rm corr}$ for the filters u, U, z, J, H, $K_{\rm s}$ (for each instrument) divided in two temperature ranges (see the text). The full table is available online as supplementary material.

	$5000\,{\rm K} < T < 10\,000\,{\rm K}$	$10\,000\,{\rm K} < T < 20\,000\,{\rm K}$
NOT+ALFOSC/NOTCam	$\Delta S_{{\rm corr},u} = 0.30$ $\Delta S_{{\rm corr},z} = 0.03$ –	$\Delta S_{{\rm corr},u} = 0.20$ $\Delta S_{{\rm corr},z} = 0.01$ –
–	–	–

Table A11. *K*-corrections expressed in magnitudes. The full table is available online as supplementary material.

Rest-frame phase [d]	*uvw*2 filter	*uvm*2 filter	*uvw*1 filter	*u* filter	*U* filter	*B* filter	*g* filter	*V* filter	*r* filter	*i* filter	*z* filter	*J* filter	*H* filter	$K_{\rm s}$ filter
−32.36	− 0.106	− 0.098	0.031	0.191	0.191	0.009	− 0.008	0.030	− 0.002	0.043	− 0.206	− 0.154	− 0.030	0.402
−25.98	− 0.100	− 0.103	0.037	0.166	0.173	− 0.015	− 0.022	0.028	0.004	0.068	− 0.203	− 0.159	− 0.030	0.148
−25.87	− 0.102	− 0.105	0.037	0.165	0.173	− 0.011	− 0.016	0.038	0.005	0.131	− 0.203	− 0.159	− 0.030	0.146
−22.96	− 0.083	− 0.055	0.080	0.129	0.137	− 0.020	− 0.023	0.028	0.013	− 0.012	− 0.202	− 0.147	− 0.033	0.089
–	–	–	–	–	–	–	–	–	–	–	–	–	–	–

Table A12. Logarithm of the bolometric luminosities integrated over the *uvw*2, *uvm*2, *uvw*1, *U*, *B*, *g*, *V*, *r*, *i*, *z*, *J*, *H*, $K_{\rm s}$, *W*1, *W*2 filters. The full table is available online as supplementary material.

Rest-frame phase [d]	$\log_{10} L_{\rm bol}$
−48.01	43.30(0.04)
−38.60	43.61(0.04)
−37.65	43.62(0.04)
−36.16	43.86(0.04)
—	–

Table A13. Spectra in Fig. 5. The full table is available online as supplementary material.

MJD	Rest-frame phase [d]	Instrumental set-up [grism/grating]	Resolution [Å]
58428.57	− 34	LCO+FLOYDS	15.5
58429.57	− 33	LCO+FLOYDS	15
58430.25	− 32	NTT+EFOSC2 [gr13]	18
58433.19	− 29	HET+LRS2	–
–	–	–	–

Note. (*)This spectrum was not included in Fig. 5 because of its poor signal-to-noise ratio, but it will be made available within the online data set (see the Data Availability statement).

[1]*European Centre for Theoretical Studies in Nuclear Physics and Related Areas (ECT*), Fondazione Bruno Kessler, Trento, Italy*
[2]*INAF - Osservatorio Astronomico di Padova, Vicolo dell'Osservatorio 5, I-35122 Padova, Italy*
[3]*Birmingham Institute for Gravitational Wave Astronomy and School of Physics and Astronomy, University of Birmingham, Birmingham B15 2TT, UK*
[4]*Institute for Astronomy, University of Edinburgh, Royal Observatory, Blackford Hill, Edinburgh EH9 3HJ, UK*
[5]*Departamento de Ciencias Físicas - Universidad Andres Bello, Avda. República 252, Santiago 8320000, Chile*
[6]*Millennium Institute of Astrophysics, Nuncio Monsenor Sótero Sanz 100, Providencia, Santiago, Chile*
[7]*INAF - Osservatorio Astronomico di Brera, Via Bianchi 46, I-23807 Merate, Italy*
[8]*Department of Astronomy, The Ohio State University, 140 W. 18th Avenue, Columbus, OH 43210, USA*
[9]*Center for Cosmology and AstroParticle Physics (CCAPP), The Ohio State University, 191 W.Woodruff Avenue, Columbus, OH 43210, USA*
[10]*IAASARS, National Observatory of Athens, 15236 Penteli, Greece*
[11]*Department of Astrophysics, Astronomy & Mechanics, Faculty of Physics, National and Kapodistrian University of Athens, 15784 Athens, Greece*
[12]*Nordic Optical Telescope, Apartado 474, E-38700 Santa Cruz de La Palma, Santa Cruz de Tenerife, Spain*
[13]*Department of Physics and Astronomy, Aarhus University, NyMunkegade 120, DK-8000 Aarhus C, Denmark*
[14]*Center for Astrophysics | Harvard & Smithsonian, 60 Garden Street, Cambridge, MA 02138-1516, USA*
[15]*School of Physics and Astronomy, University of Southampton, Southampton, Hampshire SO17 1BJ, UK*
[16]*Las Cumbres Observatory, 6740 Cortona Dr. Suite 102, Goleta, CA 93117, USA*
[17]*Department of Physics, University of California, Santa Barbara, Santa Barbara, CA 93106, USA*
[18]*Physics Department and Tsinghua Center for Astrophysics (THCA), Tsinghua University, Beijing 100084, China*
[19]*The Oskar Klein Centre, Department of Astronomy, Stockholm University, AlbaNova, SE-10691 Stockholm, Sweden*
[20]*Kavli Institute for Astronomy and Astrophysics, Peking University, Yi He Huan Road 5, Hai Dian District, Beijing 100871, China*
[21]*INFN – Sezione di Padova, Via Francesco Marzolo 8, I-35131 Padova, Italy*
[22]*Space Telescope Science Institute, 3700 San Martin Drive, Baltimore, MD 21218, USA*
[23]*Astronomical Observatory, University of Warsaw, Al. Ujazdowskie 4, PL-00-478 Warszawa, Poland*
[24]*Finnish Centre for Astronomy with ESO (FINCA), University of Turku, FI-20014 Turku, Finland*
[25]*Tuorla Observatory, Department of Physics and Astronomy, University of Turku, FI-20014 Turku, Finland*
[26]*Center for Astrophysics | Harvard & Smithsonian, 60 Garden Street, Cambridge, MA 02138-1516, USA*
[27]*The NSF AI Institute for Artificial Intelligence and Fundamental Interactions*
[28]*Steward Observatory, University of Arizona, 933 North Cherry Avenue, Tucson, AZ 85721-0065, USA*
[29]*Department of Physics and Astronomy, University of Turku, FI-20014 Turku, Finland*
[30]*Max-Planck-Institut für Astrophysik, Karl-Schwarzschild-Str 1, D-85748 Garching, Germany*
[31]*School of Physics, Trinity College Dublin, The University of Dublin, Dublin 2, Ireland*
[32]*Dipartimento di Fisica e Astronomia G. Galilei, Universitá di Padova, Vicolo dell'Osservatorio 3, I-35122 Padova, Italy*
[33]*Post Astronomy, Lexington, MA 02421, USA*
[34]*Institute of Space Sciences (ICE, CSIC), Campus UAB, Carrer de Can Magrans s/n, E-08193 Barcelona, Spain*
[35]*Department of Physics, Florida State University, 77 Chieftan Way, Tallahassee, FL 32306, USA*
[36]*Physik Department, Technische Universität München, James-Franck Str 1, D-85748 Garching, Germany*
[37]*Department of Astronomy, University of Texas at Austin, 2515 Speedway, Stop C1400, Austin, TX 78712-1205, USA*
[38]*Konkoly Observatory, CSFK, Konkoly-Thege M. út 15-17, Budapest 1121, Hungary*
[39]*Institute of Physics, ELTE Eötvös Loránd University, Pázmány Péter sétány 1/A, Budapest 1117 Hungary*
[40]*Department of Optics & Quantum Electronics, University of Szeged, Dóm tér 9, Szeged 6720, Hungary*
[41]*Astrophysics Research Centre, School of Mathematics and Physics, Queen's University Belfast, Belfast BT7 1NN, UK*

This paper has been typeset from a TEX/LATEX file prepared by the author.